The dermal skeleton of the jawless vertebrate *Trematapsis mammilata* (Osteostraci, stem-Gnathostomata)

James O'Shea[1]†, Joseph N. Keating[1,2] and Philip C. J. Donoghue[1]*

[1]School of Earth Sciences, University of Bristol, Life Sciences Building, Tyndall Avenue, Bristol BS8 1TH, UK

[2]School of Earth and Environmental Sciences, University of Manchester, Manchester, UK

†Deceased

*author for correspondence

Abstract

Osteostracans are the closest jawless relatives of jawed vertebrates, informing the gradual assembly of the vertebrate mineralised skeleton. Conflicting interpretations of their dermal skeletal histology arise from failure to account for topological variation, obscuring their significance in elucidating vertebrate skeletal evolution. To resolve this, we characterize the cranial and trunk dermal skeleton of a single individual of *Trematapsis mammilata* (Osteostraci, Thyestiida) at submicron resolution using synchrotron tomography. Our results show that the architecture of the *Trematapsis* dermal skeleton is, for the most part, conserved over the skeleton and is broadly consistent with previous histological hypotheses based on 2-dimensional thin section study. We resolve debate over the homology of the basal layer, identifying it as osteogenic acellular isopedin rather than odontogenic elasmodine or metaplastic ossification of the stratum compactum of the dermis. We find topological variation between all dermal skeletal elements studied, and particularly between the cranial and postcranial dermal skeleton. This variation can be largely explained by reduction in differentiation due to geometric constraints imposed within smaller skeletal elements, such as scales. Our description of the dermal skeleton of *Trematapsis mammilata* provides a foundation for interpreting data from cursory topological samples of dermal skeletal diversity obtained in other osteostracans. This reveals general aspects of histological structure that must be primitive for osteostracans and, likely, ancestral jawed vertebrates. Finally, we draw the distinction between hypotheses and descriptions in palaeohistology.

KEY WORDS

vertebrate, dermal, skeleton, evolution, bone, dentine, enameloid, isopedin, jawless

1 | INTRODUCTION

The vertebrate mineralized skeleton is one of the key innovations implicated in vertebrate ecological and evolutionary success (Donoghue and Purnell, 2005). It can be divided into two main components: the endoskeleton which comprises the neurocranium, splanchnocranium, axial, and appendicular skeletons, as well as the dermal skeleton which comprises the dermal skull bones, scales, teeth, fin spines and fin rays (Donoghue and Sansom, 2002). The dermal skeleton forms within the dermis and results from inductive interactions between mesenchyme and an overlying epithelium (Hall, 2014; Sire and Huysseune, 2003) and can be divided further into the odontogenic and skeletogenic components (Smith and Hall, 1993). The former develops from morphogenetic units known as odontodes that are represented by teeth, placoid scales and tubercles on dermal bone (Donoghue, 2002; Ørvig, 1967; 1977; Reif, 1982). These structures all share a basal bone of attachment, dentine and an overlying hypermineralised cap of enamel or enameloid (Ørvig, 1967; Smith and Hall, 1993). The skeletogenic component gives rise to the bony plates underlying the odontodes (Smith and Hall, 1993). Historically, many hypotheses about the evolution of the dermal skeleton have focussed on the stratigraphic sequence of appearance. Crown gnathostomes ancestrally possessed a fully developed dermal skeleton of cellular bone overlain by odontodes (dermal tooth-like structures) (Donoghue and Sansom, 2002; Giles et al., 2013; Keating and Donoghue, 2016; Keating et al., 2015; Keating et al., 2018; Sire et al., 2009). In contrast, extant jawless vertebrates and non-vertebrate chordates entirely lack a mineralised skeleton. If only looking at the record of living vertebrates, the gnathostome stem represents an enormous gap in our understanding of how the dermal skeleton arose. Conveniently, an array of extinct jawless skeletonizing vertebrates (Pteraspidimorphi, Anaspida, Thelodonti, Galeaspida and Osteostraci) collectively referred to as ‘ostracoderms’, along with the jawed ‘placoderms’, fall along the gnathostome stem and bridge this phylogenetic gap (Fig. 1) (Donoghue et al., 2014). Stem-gnathostomes variously display a tripartite dermal skeleton, with an odontogenic superficial layer underlain by an osteogenic vascular middle layer and lamellar basal layer, however, the recent discovery that anaspids lack a true middle layer has led to the suggestion that this was absent in the ancestral vertebrate dermal skeleton (Keating and Donoghue, 2016). Since its conception, the evolution of the dermal skeleton is most concisely explained as the relative gain and loss of odontogenic and skeletogenic components. For example, the dermal skeleton of thelodonts consists solely of odontogenic placoid-like scales; the skeletogenic component is effectively absent. By contrast, galeaspids have a well-developed skeletogenic component, but the odontogenic component is probably absent (Wang et al., 2005).

Osteostraci (Wenlock - Fransian) are the closest jawless relatives of jawed vertebrates, sharing with crown gnathostomes, to the exclusion of other ‘ostracoderms’, sclerotic rings, an ossified sclera, paired pectoral fins with an internal skeletal support, cellular bone and ossification of the braincase

with perichondral bone (Janvier, 1984; 1996; 2004). Osteostracans therefore represent an important grade in the evolution of the vertebrate skeleton, but despite being well-studied, their dermal skeletal histology is poorly understood within an evolutionary context and conflicting interpretations over tissue homologies remain (e.g. Sire et al., 2009). To establish a framework for interpreting the osteostracan dermal skeleton which accounts for topological variation in histology and to investigate their significance in the origins of the crown-gnathostome skeleton, we have focussed on a single articulated specimen of *Trematapis mammilata* Patten (Figure 3), investigated using Synchrotron Radiation X-ray Tomographic Microscopy (SRXTM). The dermal skeletal histology of *Trematapis* is unusual compared many other osteostracans, however, exceptional preservation and availability of articulated specimens for sampling makes it ideal for establishing a point of comparison with other osteostracan taxa. In addition, *Trematapis* has an extensive body of literature surrounding its dermal skeleton, including a variety of morphological and homological interpretations which can be tested. Indeed *Trematapis* has been central to many discussions of the osteostracan dermal skeleton within the context of tissue homologies and growth (Denison, 1951; 1963; Donoghue et al., 2006; Gross, 1956; Ørvig, 1967; Patten, 1912; Qu et al., 2015; Sire et al., 2009).

2 | PREVIOUS HISTOLOGICAL STUDIES OF *TREMATASPIS*

There are currently six recognised species of *Trematapis* (Märss et al., 2015), the best studied of which are *T. mammilata* and *T. schmidtii*. Like all osteostracans, *Trematapis* has a three-layered exoskeleton, like all osteostracans and most stem-gnathostomes. The superficial layer is smooth and has a continuous hypermineralised cap. Underneath this is a layer of tissue with embedded, or partially embedded, polarised cell lacunae and multiple radiating canaliculi characteristic of mesodentine (Ørvig, 1967). This has been interpreted as a phylogenetic intermediate between bone and dentine (Denison, 1947; Gross, 1935; 1956; Ørvig, 1951; 1967; Stensiö, 1927; 1932). Gross (1956) interpreted the superficial tissue of the dermal skeleton in *T. schmidti* as bone and that of *T. mammilata* as dentine, based on differences in lacuna polarity. He figured multiple ontogenetic stages of *T. mammilata* showing the progressive retreat of the odontoblasts towards the subepidermal vascular plexus (a name applied to canals underlying the dentine by Stensiö, 1932), and the progressive infilling of pulp cavity extensions to form dentine canaliculi (Gross, 1956). Donoghue et al. (2006) noted that the limited phylogenetic distribution of this tissue suggests that it is not a bone-dentine intermediate but, rather, a derivative of orthodentine. The hypermineralised tissue capping the superficial layer of the dermal skeleton has been interpreted as enamel or an enamel-like tissue (Denison, 1947; Stensiö, 1927). The hypermineralised capping layer in many fish is not purely ectodermal (as in true enamel) but has mesenchymal and ectodermal contributions (Hall,

2015), hence this tissue has conventionally been referred to as enameloid (Ørvig, 1967). Enameloid is present in actinopterygians and chondrichthyans, where its development has been investigated and its homology disputed (Gillis and Donoghue, 2007). Enameloid is also identified in extinct clades such as heterostracans, anaspids, thelodonts, and placoderms, as well as osteostracans (Gillis and Donoghue, 2007), though it shows great variation in microstructure and its homology is difficult to test.

The middle layer of *Trememataspis* is highly vascular and is universally interpreted as cellular bone, with osteocytes and lamellae arranged concentrically around the canals (Denison, 1947; 1963; Gross, 1935; 1956; Patten, 1912; Qu et al., 2015; Stensiö, 1927). The basal layer of *Trememataspis* and other osteostracans has been interpreted as cellular bone (Denison, 1963 Ørvig, 1967 #1423; Gross, 1935; Patten, 1912; Stensiö, 1927), isopedin (Donoghue et al., 2006; Gross, 1956; 1968a; b), elasmodine or ossification of the stratum compactum (Sire et al., 2009). Here we follow Francillon-Vieillot et al. (1990) in using the term isopedin to refer to any basal plywood-like lamellar tissue of the dermal skeleton, making it purely structural. The term elasmodine encompasses the poorly mineralised plywood-like tissue found in the scale bases of extant polypterids, amiids, coelacanths and dipnoans (Sire et al., 2009). Putative cell spaces in the basal layer occur only between juxtaposed fibre bundles (Gross, 1935), with canaliculi extending horizontally along the same lamella and vertically between lamellae (Denison, 1947; Gross, 1956). Reconstructions of the spaces between the juxtaposed fibre bundles infer a six pointed star shape resulting from the intersection of three orthogonal planes (Gross, 1956). This led Wang et al. (2005) to suggest that these spaces simply result from the geometry of the intersecting fibre bundles.

The mesh canals of *Trememataspis* (sensu Gross, 1956) represent a polygonal network throughout the middle layer, giving rise to pores in the superficial surface (Denison, 1947; Gross, 1935; 1956; Patten, 1912; Stensiö, 1927; 1932). Stensiö (1927; 1932) hypothesised that these functioned in mucus conduction, however, a sensory interpretation was also suggested by Stensiö and this has been favoured by most authors (Bölau, 1951; Denison, 1947; Gross, 1935; 1956; Qu et al., 2015), but see (Wängsjö, 1952). Stensiö (1927) was the first to homologise these with the inter- and intra-areal canals of other osteostracans. Such structures may be present as grooves (Fig. 2B) or be completely enclosed and show extensive variation throughout the Osteostraci (Stensiö, 1932). The mesh canals of *Trememataspis* are divided into upper and lower divisions by thin sieve plates (Denison, 1947). Bölau (1951) and Gross (1956) later noted that these exhibit perforations representing the only connections between the upper mesh canals and the remaining canals of the dermal skeleton. Stensiö (1927) described a vascular network beneath the superficial layer which supplied the

overlying dentine lacunae; based on comparisons to lampreys, he termed it the subepidermal vascular plexus. Both the subepidermal vascular plexus and the lower mesh canals connect to a lower canal network of the middle layer, described by Gross (1935) as the "lower horizontal net of the subepidermal vascular plexus" (translation by Wängsjö, 1946) and later homologised to the radiating canals of other osteostracans (Denison, 1947; Wängsjö, 1946). The radiating canals were observed to connect to large cavities in the basal layer which correspond to the overlying polygons (Denison, 1947; Gross, 1956). These cavities truncate fibre bundles and have been interpreted as vascular sinuses which contract during growth (Denison, 1947), or occur as a result of resorption (Denison, 1952; Gross, 1956).

Qu et al. (2015) provided the most recent description of osteostracan dermal vasculature, focussing on a partial scan of a trunk scale from *Trematapis schmidti* and the thyestiid *Oeselaspis pustulata*. Importantly they used 3D SRXTM data to visualise the canals, permitting tests of previous hypotheses for the 3D arrangement of these spaces based on 2D thin sections (e.g. T. mammilata Fig. 2A Denison, 1947). Differences observed between the scale scan and Denison's model were used to call into question the veracity of the traditional approach of deriving 3D hypotheses of histological structure based on approximately 2D sections. For example, Qu et al. (2015) note that the lower mesh canals and lower canal network form a geometrically continuous tree-like system. By contrast the upper mesh canals are smooth and regular. This indicates that the lower and upper mesh canals are fundamentally distinct, rather than components of the same canal system divided in two, as advocated by Denison (1947). In addition, the basal cavities are restricted to the anterior portion of the scale they studied and show no correspondence to the overlying mesh canals. This lead Qu et al. (2015) to reject Denison's hypothesis that the basal cavities and polygons show correspondence (Denison, 1947). However, Denison's model cannot be rejected on this basis, not least since his hypothesis of 3D histological structure was based on *T. mammilata*, making inter-species variation a possible source of this disparity. Secondly, Denison (1947) focussed on the histology of the headshield while the scale studied by Qu *et al* (2015) was from the post-cranial trunk dermal skeleton, introducing the possibility that the differences observed result from topological variation in dermal skeletal structure and development. Thirdly, the limitation of the study by Qu *et al* (2015), to a partial scan of a single scale, introduces the possibility that population level variation within the available sample of scales (e.g. ontogenetic variation) is the cause of the differences observed. For example Denison (1947) notes varying stages of basal cavity development between specimens of *T. mammilata*.

In order to test existing hypotheses on the structure of the dermal skeleton in *Trematapsis mammailata* (Denison, 1947; Gross, 1935; 1956; Qu et al., 2015; Wängsjö, 1952) and resolve controversy over tissue homologies (Sire et al., 2009), we characterised topological variation in the histology of the dermal skeleton in a single articulated individual of *T. mammilata* using SRXTM.

3 | MATERIALS AND METHODS

The material examined comes from a single articulated specimen of *Trematapsis mammilata* NHMUK P20008; Figure 3) from the Upper Silurian Himmiste beds of Saaremaa (Ludlow) (Märss et al., 2015). The specimen is not complete; the rostral portion of the headshield is missing, as is the caudal end of the trunk. It was originally only partially exposed within the original limestone sediment (Fig 3A) and so, prior to sampling components of the skeleton for analysis, all but the exposed surface of the specimen was encased in wax prior to acid dissolution of the carbonate sediment using 6-8% buffered acetic acid following the established protocol for the recovery of phosphatic microfossils (Jeppsson et al., 1999). Once the specimen was exposed (Figure 3B) sufficiently to facilitate all of the key components of the dermal skeleton, the sample was repeatedly washed overnight in pH neutral water. Scales and headshield fragments were either isolated through the process of matrix dissolution or else through mechanical removal with a picking brush or entomological needle mounted in a pin vice.

The dorsal headshield material comes from a smooth region, a region with tubercles and the posterior angle. Dorsal, medial, and ventral scales were sampled from the trunk and caudal regions (Fig. 3). Synchrotron Radiation X-ray Tomographic Microscopy of the samples were performed at the X04SA TOMCAT beamline at the Swiss Light Source, Paul-Scherrer Institute, Villigen, Switzerland. Specimens were measured using x4, x10, x20, and x40 objective lenses (yielding reconstructed tomographic data with voxel dimensions of 1.625 µm, 0.65 µm, 0.325 µm and 0.1625µm, respectively), at energy levels of 18-35 keV and exposure times of 75-2000 ms. 1501 projections were taken equi-anglularly through 180^{o} of rotation within the beam. Projections were post-processed and rearranged into flat- and dark-field-corrected sinograms, and reconstruction was performed on a 60-core Linux PC farm, using a highly optimized routine based on the Fourier transform method and a regridding procedure (Marone and Stampanoni, 2012). Slice data were analysed and manipulated using Avizo 8.0 (FEI Visualisation Sciences Group 2013). Histological sections were generated either as single tomographic slices using the orthoslice and slice modules or as volume rendered virtual thin sections ranging from 10 to 86 slices thick. Canals and spaces within *T. mammilata* were isolated using the greyscale threshold tool in the segmentation editor and visualised using the surface

module. Putative cell spaces were isolated using island removal. Correction of island removal artefacts and sediment infill was performed by manually tracing canals at regular intervals through the 3D data stack and interpolation across slices. The tomographic data and AVIZO network files on which this study is based are available in the Bristol Digital Repository: http://dx.doi.org/XXXX (to be completed on acceptance).

4 | RESULTS

All elements of the dermal skeleton consist of three tissue layers, with contribution from these tissue layers varying across the body. The superficial layer consists of cellular mineralised tissue pervaded by polarised canaliculi. This is overlain by a hypermineralised cap. The middle layer contains abundant lacunae and numerous canals, with lamellae arranged concentrically around the canals. The basal layer consists of a plywood-like lamellar tissue. For descriptive purposes the canal system of the dermal skeleton has been broken into five components. The terminology adopted here is modified from that of previous authors to avoid functional assumptions. The superficial canal network lies just beneath the superficial layer (subepidermal vascular plexus of (Denison, 1947; Stensiö, 1927). In the middle layer beneath this is a polygonal network of mesh canals with upper and lower divisions separated by sieve plates (sensory canals of Denison, 1947; Maschenkanal of Gross, 1956). The upper mesh canals connect to the superficial surface via pore cavities which ascend to form pore canals (Porenkanal of Gross, 1956). At the level of the lower mesh canals there is a less regular lower canal network (lower vascular plexus of Denison, 1947). Large cavities occupy the basal layer (vascular sinus of Denison, 1947). Each polygonal unit cell of the mesh canal contains a repeating pattern of these vascular components.

4.1 | *Trememataspis mammilata* headshield general structure

Three portions of the headshield were analysed; a smooth portion (approx. 320µm thick), a smooth portion bearing mammillae (small rounded tubercles) (approx. 220µm thick), and the posterior medial tip of the headshield (over 880µm thick).

The superficial layer (22% total thickness in the smooth region) is continuous, regularly perforated by circular pores (32µm in diameter) and overlain by a thin veneer of highly attenuating hypermineralised tissue (approx. 9µm thick) which extends into the upper portions of the pore cavities (for clearer demonstration of this see scales) (Fig. 4A). The upper canal network lies just beneath the superficial layer and gives rise to polarised lacunae (approx. 30µm tall, 12µm wide). The

lacunae (Fig. 4A-B; 5A-C) anastomose with one another via thin canaliculi (approx. 3µm thick) and extend superficially for approximately 56% of the superficial thickness. Some of these lacunae are completely enclosed within in mineralised tissue. Above this, the lacunae constrict to form polarised canaliculi (approx. 2µm thick) which bifurcate sharply up to four times, but rarely anastomose. On approaching the surface, these bend to run almost surface parallel. Generally, these oblique canaliculi fan out in the horizontal plane. Close to the pore canals, the canaliculi lean over towards the lacuna (Fig. 4B).

Mammillae consist of thickened superficial tissue (50% total thickness) including the hypermineralised cap (Fig. 8A) (approx. 19µm vs 7.5µm in adjacent regions). Towards the centre of a mammilla, the ascending canaliculi are increasingly polarised (Fig. 8A-B). Tubercles form a sagittal row leading to the posterior medial tip of the headshield and here the hypermineralised cap is at its thickest (39µm). At the headshield margin, the superficial and middle layers extend onto the interior surface before stopping abruptly as an embayed ledge (Fig. 9A). Medial to these embayments is a row of conical tubercles (one measured 86µm tall, 95µm wide at the base) which runs parallel to the posterior margin of the headshield. The tubercles are composed of superficial tissue containing polarised lacunae and a hypermineralised cap (Fig. 9B). Cavities in the basal tissue on which they sit correspond to each tubercle and supply the polarised lacunae (Fig. 9F).

The middle layer (14% of total thickness in the smooth region) consists of lamellar tissue with abundant lenticular lacunae. The lamellae and lacunae are arranged concentrically around the mesh canals and the lower canal network. Concentric lamellae stop at connections between the lower mesh canals and the lower canal network and often thin out around the margins of these canals (Fig. 4A). The 3D data reveals that the lacunae are oblate sphaeroids, flattened parallel to the surrounding lamellae (long axis approx. 11µm) (Fig. 5A, D). The lacunae connect to each other with radiating canaliculi. Some connect to the lower canal network and lower mesh canals, but there are no lacunar connections to the upper mesh canals. The sieve plates (approx. 3.6µm thick) separating the upper and lower mesh canals occur in all headshield regions examined (Fig. 4C). In the smooth region, the perforations are wider and more polygonal beneath the pore canals (approx. 6µm), but smaller and more circular away from them (approx. 4µm). High resolution in the region with mammillae shows that the sieve plates are smooth on the superficial surface, but roughened on the inner surface. This results from the semi-circular cross section of the thin trabeculae bounding the perforations (approx. 4.4µm thick), where the curved sides face basally. When viewed from a basal perspective, the trabeculae of the sieve plates extend and gradually merge into the lateral surfaces of the lower mesh

canals, bounding cavities on the canal surfaces which resemble the perforations on the sieve pates (Fig. 8D). Ridges continuing from these trabeculae may extend around the lower mesh canals.

The basal layer ranges extensively in relative thickness, being especially thin (approx. 18% total thickness) in the region with mammillae but especially thick (approx. 68%) near the posterior margin. It exhibits a plywood-like architecture of successive lamellae one fibre bundle thick and in the smooth region can be divided into three levels characterised by differing fibre bundle dimensions (Fig. 4A, D). The upper level (fibre bundles approx. 8µm thick) occurs mostly above the large cavities characteristic of the basal layer, the middle level (fibre bundles approx. 19µm thick) forms the lateral surfaces of the cavities and the lower level (fibre bundles approx. 12µm thick) occurs beneath the cavities. The fibre bundles are oval to rectangular in cross section. 3D reconstruction of overlying fibre bundles in the lower level reveals that they intersect obliquely, anastomose horizontally, and continue uninterrupted for at least 576µm (Fig. 5H-I), however, bundles in the middle level are regularly cross cut by the cavities. Fibre bundle orientation repeats on alternating lamellae, with an average angle between overlying fibre bundles of 76^{o}. Lacuna-like spaces in the upper portion of the basal layer (approx. 18µm long and 3µm thick) (Fig. 5E) are typically flattened horizontally and extend in the direction of the overlying and/or underlying fibre bundles. The fibre bundles of the middle and lower levels are less tightly packed resulting in highly elongate criss-crossing spaces (up to 140µm long) occurring between adjacent bundles (Fig. 5F-G). Expansions correspond to the intersections of fibre bundle gaps in two superimposed lamellae (3-8µm diameter) and spaces separated by lamellae communicate vertically between fibre bundles. In the posterior margin of the headshield the basal tissue is especially thick and consists of trabeculae (Fig. 9C, D, G). Oblique sections suggest that the internal portion consists of well-organized successive lamellae with a plywood-like architecture. However sandwiched between this and the middle layer is a cancellous portion with spheritic mineralization (Fig. 9F). At the margin of the plate, the basal layers extends around the rim, sealing the middle layer to meet the superficial layer (Fig. 9C).

The upper mesh canals form a planar polygonal network in the upper middle layer and lower superficial layer (Figs. 6A, 7A-B, D). Their surface is uniquely smooth and regular. In cross section (approx. 40µm wide and 30µm tall), the upper mesh canals are semi-circular, with the flattened basal edge formed by the underlying sieve plates. The perforations in the sieve plates represent the only connections between the upper mesh canals and the surrounding spaces. Each polygon has 4-7 vertices with 6 being the most common number. Flask-shaped cavities (approximately 110µm at broadest width, 100µm from base to top) represent expansions of the mesh canal system (Fig. 4A, Fig. 7) and mostly occur at the vertices, but sometimes along the edges of the polygons. Pore canals

ascend from the cavities and narrow before opening onto the superficial surface to form pores (average spacing 351µm). The upper mesh canals often arch upwards above the junctions between the lower mesh canals and the larger canals of the lower canal network. The lower mesh canals track the upper mesh canals through the lower part of the middle layer and have an irregular surface with frequent changes in diameter and cross sectional shape, although this is generally oval (approx. 60µm wide, 25µm tall). There are regular connections between the lower mesh canals and the lower canal network and very rarely to the cavities of the basal layer. Both the upper and lower mesh canals follow the superficial and middle layers around the posterior margin of the headshield onto the interior surface and open at the embayed ledge formed where these layers terminate (Fig 9D, cross section shows where upper and lower mesh canals open onto the interior surface of the headshield).

The lower canal network is almost indistinguishable from the lower mesh canals when viewed from the base (Fig. 6D). It represents an amalgamation of spaces with differing geometries and relations to other nearby canals, but all are united by their complete or partial occurrence within the lower part of the middle layer. The spaces have an irregular surface and an oval cross section. On a large scale wide primary canals (approx. 70µm in diameter) originate within the polygonal centres from the underlying basal cancellae. These then ramify horizontally, connecting to and emerging from the lower mesh canals as they traverse multiple polygons (Fig. 6D). Superficially they send connections to the superficial canal network. Eventually the primary canals grade imperceptibly into the remainder of the lower canal network and lower mesh canals. The large diameter of these canals means that their upper surface commonly reaches the base of the superficial layer where they connect to overlying polarised lacunae. In other cases, the canals rising from the basal cancellae cannot be seen to traverse polygonal boundaries instead rising to supply the superficial canal network (Fig. 7E). The lower mesh canals regularly send out narrow horizontal canals towards the centre of each polygon (approx. 35µm in diameter) (Fig. 7D). These turn superficially to form a right angle in transverse section and connect to the superficial canal network (Fig. 5B). Each polygon has at least one connection between the basal cancellae and the lower canal network. The superficial canal network occupies the upper middle and lower superficial layers, giving rise to numerous polarised lacunae. It has an irregular circular cross section (approx. 45µm in diameter) and connects via vertical canals to the lower canal network. There are no connections between the superficial canal networks of adjacent polygons. When viewed from above, the superficial canal network forms a broken ring bounded externally by the upper mesh canals (Fig. 6A, 7D). In some of the smaller polygons this ring is complete.

The basal cavities are oblate spheroids (approx. 50% total thickness) with grooves and ridges corresponding to the lamellae which they intersect (Figs 4A, D, 6B, 7C). Grooves correspond to a lamella with fibre bundles perpendicular to the cavity surface, whereas ridges correspond to a lamella with fibre bundles tangential to the cavity surface. The basal cavities are patterned such that most mesh canal polygons have a single underlying cavity, however this correspondence is not perfect and there may be more than one cavity in each polygon or cavities may straddle polygonal boundaries (Fig 6. B-C). Superficially, the cavities connect to the lower canal network and more rarely the lower mesh canals. Basally, the cavities connect via vertical canals to the interior of the headshield, however, the morphology of these canals is often unclear due to post mortem compaction related deformation of the basal layers. Connections between adjacent cavities vary, with some exhibiting very wide connections and others not connecting at all. Along the horizontal plane, the cavities are arranged into parallel rows (Fig. 6E), with cavities within these rows showing the widest connections. Around the posterior margin canals and cavities in the basal layer are arranged in concentric rows, with one row supplying the outer row of tubercles which occur on the internal surface of the headshield.

4.2 | Headshield tubercles

The sieve plates (approx. 6.7µm thick, perforations approx. 6.9µm in diameter) are well preserved in this region (Fig. 8C, E). They are smooth on the superficial surface, but rougher on the basal surface. This results from the semi-circular cross section of the thin trabeculae bounding the perforations (approximately 4.4µm thick), where the curved sides face basally. When viewed from a basal perspective the trabeculae of the sieve plates extend and gradually merge into the lateral surfaces of the (lower mesh canals), bounding cavities on the canal surfaces which resemble the perforations on the sieve pates (Fig. 8D). Ridges continuing from these trabeculae may extend around the canals. The basal layer (here 15% total thickness) is poorly developed compared to the remainder of the headshield.

4.3 | Posterior margin of the headshield

In the superficial layer (approx. 8% total thickness) the hypermineralised cap is especially thick (39µm). The superficial and middle layers extend onto the interior surface of the headshield before abruptly stopping as an embayed margin (Fig. 9A). Mesial to these embayments is a row of conical tubercles (one measured 86µm tall, 95µm wide at the base) which runs parallel to the posterior margin of the headshield. The tubercles are composed of superficial tissue containing polarised lacunae and a hypermineralised cap (Fig. 9B). Cavities in the basal tissue correspond to each tubercle and supply the polarised lacunae (Fig. 9F). The basal and middle layers exhibit spheritic

mineralization, locally organised trabeculae (up to 80% total thickness) (Fig. 9C, D, G). The basal layer extends around the rim of the headshield to seal the middle layer, meeting the superficial layer at the embayed ledge (Fig. 9C). The upper mesh canals form a polygonal meshwork (Fig. 9E). On the internal surface of the headshield where the superficial and middle layers are present, the mesh canals open at the point where these layers terminate as an embayed ledge. Canals and cavities in the basal layer are arranged in rows concentric to the posterior margin of the headshield, with one row supplying the outer row of tubercles.

4.4 | Trunk scales

4.4.1 | General structure

All scales have the same general external morphology. A smooth continuous superficial layer forms the scale field which is perforated by numerous pores. Beneath this is a constriction forming the scale neck (Märss et al. 2014) which corresponds to the middle layer. The basal portion of the scale is extended anteriorly to form the overlapped region. Scales range in shape from rhombic on the trunk to diamond shaped on the caudal fin. Our description of the scales focuses on the caudal scales (Fig. 10) which exhibit an intermediate morphology between the rhombic caudal scales (Fig. 13 D-F) and diamond-shaped caudal scales (Fig 13. A-C). The anterior margin is identified by the presence of the overlapped region, and the lower “free” margin is identified as the overhanging region which extends orthogonally from it.

The superficial layer (30% total thickness, but much thicker where middle layer is absent) pervaded by polarised lacunae and canaliculi which permeate the overlying hypermineralised cap (< 1% total thickness; ~ 2.1µm thick) (Fig. 10A). The lacunae and canaliculi are surrounded by three concentric phases of different attenuation (Fig. 13A-G) and the hypermineralised cap extends into the pore cavities (Fig. 13G). In the horizontal plane, most canaliculi extend towards the posterior margin of the scale, however, some canaliculi extend towards the anterior and lower margins (Fig. 10C). The superficial layer extends onto the underside of the posterior and lower margins of the scale, giving rise to a row of rounded tubercles containing polarised lacunae and a hypermineralised cap (approx. 4.2µm thick) (Fig. 10E). The superficial layer stops as an embayed ridge on the underside of the posterior margin (see mid ventral scales)**.** As in the headshield, the middle layer (20% total thickness) consists of concentrically arranged lamellae bounding lenticular lacunae. It is discontinuous, almost exclusively surrounding the mesh canals (Fig. 10A). The sieve plates are continuous with lamellae surrounding the lower mesh canals. As in the headshield, their perforations become smaller and more rounded away from the pore cavities. The basal layer (50% total thickness) is similar to that of the headshield. It consists of a lamellar plywood-like tissue, with fibre bundles cross cut by basal

cavities. Fibre bundles increase in thickness basally (5.4-14µm) and become less densely packed. Between the fibre bundles are spaces that appear lenticular in transverse section and cross-shaped in horizontal section, exhibiting the same geometric relationship to the fibre bundles as seen in the headshield. A zone of low attenuation extends from the superficial layer onto the upper surface of the overlapped portion of the scale. In this region the fibre bundles are poorly defined.

The canals of the trunk and caudal scales contain all of the components seen in the headshield, with the vascular pattern repeating within regions defined by the mesh canals and the edges of the scale (Fig. 11). One complete polygon is observed in the 3D reconstruction of the intermediate caudal scale. Despite much of the upper margin of the scale being partially broken, the smooth anterior portion of this margin indicates that only a small portion of the scale was lost and that most of the canal system is preserved. The upper mesh canals (approx. 20µm tall, 40µm wide) extend into the superficial layer. The complete polygon is small and has six vertices. It sends two straight mesh canals towards the anterior margin which open beneath the superficial layer in the scale neck. One mesh canal extends towards the lower margin of the scale and one towards the posterior margin, both opening on the scale underside (Fig. 11E). Near the upper margin, two canals form a partial polygon open onto the scale side, however, this margin is broken so the true openings of the canals are absent. Unlike the headshield, the pore canals are inclined along the diagonal of the scale (Fig. 11B). No arching of the upper mesh canals is observed. The lower mesh canals (approx. 20µm tall, 40µm wide) occur within the middle layer of the scale and are indistinguishable from the lower canal network in basal view (Fig. 11F). One large lower mesh canal opens onto the underside of the posterior scale margin and ramifies comparably to the primary canals of the headshield. The lower mesh canals connect to the basal cavities more frequently in the scale than they do in the headshield. They continuously track the upper mesh canals except for two breaks, however this results from infilling of the cavity with sediment. The lower canal network (approx. 50µm tall, 60µm wide) extends further into the superficial layer than seen in the headshield, with their upper surfaces giving rise to more polarised lacunae. The lower canal network anastomoses extensively with the lower mesh canals, connects to the basal cavities, and opens onto all four margins of the scale. Like the headshield, narrow canals (approx. 16µm in diameter) extend from the lower mesh canals towards the polygonal centres and then turn upwards to supply the superficial canal network. Unlike the headshield, the polygonal region lacks connections between the lower canal network and the basal cavities. The superficial canal network is poorly differentiated from the lower canal network, however, these canals are distinguished by their small diameter (approx. 30µm), restriction to the superficial layer and loop-like shape when viewed from above (Fig. 11E). Like the headshield, the superficial canal network does not pass over the upper mesh canals. In the posterior and lower

portions of the scale, these canals lose their ring-like configuration and extend towards the margins of the scale where they send connections to the underside of the scale. The basal cavities (Fig. 11A) occur beneath the scale field and within the overlapped region, opening onto the lower surface of the scale (approx. 80µm tall). The cavities occupy a far greater volume of the basal layer and show rough correspondence to the mesh canals.

4.4.2 | Dorsal trunk scales

The dorsal trunk scales achieve a maximum thickness of approximately 730µm). In the superficial layer, each lacuna is surrounded by a highly attenuating phase (la1; Fig 13E, G blue and green) which is continuous with the material encompassing the superficial canal network. This inner lamella is concentrically surrounded by a darker phase (la2; Fig. 13E, G pink) superficially which seems to contact the canaliculi as la1 thins out away from the superficial canal network. This lamella exhibits especially low attenuation just beneath the capping tissue, but seems absent once the canaliculi pervade it. The highly attenuating hypermineralised cap (la3; Fig. 13G white) partially surrounds the dark lamellae on its basal surface. In addition this capping tissue extends into the pore canals but thins out before reaching their base. In the middle layer lamellae variously surround the upper mesh canal and part of the lower mesh canal, the lower mesh canal only or the upper mesh canal only. The lamellae surrounding the upper mesh canal exhibit low attenuation and appear to be continuous with la2 of the superficial layer (Fig. 13C-G). When these extend to the lower mesh canal they appear to be cut across by concentric lamellae of the lower canal network where it connects to the lower mesh canal (Fig. 13C, E, G). This termination is often sharp and is marked by a highly attenuating ring around the lower canal network lamellae (Fig. 13C). The lamellae surrounding the lower mesh canal are highly attenuating and may be encompassed by lamellae surrounding the upper mesh canal. They appear continuous with la1 as well as the lamellae around the lower canal network. The basal layer is exceptionally thick (70% total thickness), with fibre bundle diameter increasing basally. Much of the overlapped region forms a low attenuation phase with indistinct fibre bundles and appears continuous with the superficial layer. In one instance, a canal leading from a basal cancellum invades this low attenuation region, surrounded by high attenuation tissue similar to, and continuous with, the rest of the basal layer. A concentric arrangement of lamellae occurs around the small spaces between the fibre bundles. No enclosed polygon is formed by the mesh canals (Fig. 12B). The basal layer is entirely hollow (Fig. 13G).

4.4.3 Diamond shaped caudal trunk scales

Overall, these scales achieve a maximum thickness of 320µm (Fig. 13A-C). The superficial layer is well developed. The middle layer is especially discontinuous, poorly developed and restricted to the mesh

canals, overlapping extensively with the superficial layer. The basal layer is hollow. Only a single pore canal occurs in the centre of the scale field and no polygons are present. The mesh canals extend away from the pore cavity to all four sides of the scale.

4.4.4 | Rhombic mid ventral trunk scales and rhombic caudal trunk scales

These achieve a maximum thickness of 390µm an 440µm, respectively (Fig. 13D-I), exhibit extensive overlap, and are much larger than the diamond-shaped trunk scales. The superficial layer extends over the posterior margin giving rise to a row of conical tubercles (Fig. 13E). Viewed externally, there is an embayed ledge corresponding to the termination of the superficial layer. The tubercles occur near posteriorly-extending canals from the superficial canal network. The superficial and middle layers each comprise 15-25% of the scale thickness, with the middle layer developed to encompass little more than the upper and lower mesh canals. In the mid ventral trunk scales, fibre bundles curve upwards towards the overlapped surface. In much of the overlapped area the tissue becomes less highly attenuating and the fibre bundles less distinct. A similar situation occurs on the posterior underside of the scale. Canal geometry is consistent with the diamond shaped caudal trunk scale, although multiple mesh canal polygons occur along the scale long axis. The basal cavities are well developed under the scale field and within the overlapped region. They open onto the basal surface of the scale and the superficial surface of the overlapped region.

5 | DISCUSSION

5.1 | Variation within the dermal skeleton of *Trematapsis mammilata* and comparison to previous interpretations

Both the headshield and scales show three main layers: a continuous superficial layer pervaded by polarised canaliculi overlain by a hypermineralised cap which extends into the pore canals (e.g. Fig. 10A, 13G), a middle layer marked by concentrically arranged lamellae and lenticular lacunae and a basal layer of plywood-like lamellar tissue pervaded by large cavities. In the scales, three phases of differing attenuation (la1-3; Fig. 13) concentrically surround the polarised lacunae and superficial canal network. In addition, these are continuous with the lamellae surrounding the canals of the middle layer. The same three phases may also be present in the headshield (Fig. 4A). The superficial layer is thickest on the headshield where tubercles are present. It also forms the entire thickness of the posterior and lower scale margins. Similarly, the superficial layer extends over the posterior margins of the headshield and scales, terminating as an embayed ridge. The middle layer is best

developed on the headshield, but it is all but absent in the posterior-most caudal trunk scales, exclusively surrounding the mesh canals and interrupted regularly by superficial tissue. The basal layer is least developed in the tuberculated headshield region. The unusual basal tissue in the posterior margin of the headshield may be partly endoskeletal (see below). All scales have a thick basal layer, but this is almost hollow due to extensive cavities. The superficial portion of the overlapped region in the scales is exhibits low attenuation and appears continuous with the superficial layer, although the tissue structure is most comparable with that of the basal layer.

Both the headshield and scales contain smooth and regular upper mesh canals. The smallest caudal scales lack polygons altogether. In the headshield and scales irregular lower mesh canals are separated from the upper mesh canals by a sieve plate which is continuous with the walls of the lower mesh canals. The superficial canal network in the upper middle and superficial layers never passes over the mesh canals and connects basally to a horizontally branching lower canal network. The lower mesh canals and lower canal network are indistinguishable in basal view. In the scales, the superficial and lower canal networks are less differentiated than those of the headshield and extend towards all four scale margins. The basal cavities always connect to the overlying lower canals and lower mesh canals of the middle layer. On the smooth portion of the headshield they are arranged in rows and show approximate 1-1 correspondence to the overlying polygons. A less regular correspondence is observed in the intermediate caudal trunk scale. The basal cavities are always extremely large in the trunk scales, occupying almost the entire basal layer. In the region with tubercles the cavities are truncated from top to bottom due to the thinness of the basal layer. In the posterior portion of the headshield canals and cavities co-occur in the endoskeleton with the cavities arranged in concentric rows.

Broadly these observations support the 3D models proposed by previous authors based on 2D data (Denison, 1947; Gross, 1956), however, the use of 3D SRXTM data reveals more variation on the common themes described and some contradictions are addressed. Denison's observation of 1-1 correspondence between the basal cancellae and the mesh canal polygons in the headshield of *Trematapsis* is confirmed and extended to the scales, however here it is less precise. This indicates that the conflicting observation of Qu *et al.* (2015) results from topological variation between the trunk and headshield. The geometry of the primary ramifying canals found by Qu *et al.* (2015) was not noted in 2D studies, but the above data reveal their presence in the headshield and a similar ramifying geometry in the lower mesh canals and lower canal network system in the scales. Similarly to Qu *et al.* (2015), we find no evidence for a fundamental distinction between the lower mesh canals and lower canal network, both of which form a continuous network with a roughened texture.

Unlike Denison (1947), none of the scans recorded the lower canal network passing under the lower mesh canals, instead the lower canal network and lower mesh canals anastomose within the same plane. However some of the samples analysed by Denison (1947) had a far thicker middle layer than any of those described above. The putative lacunae of the basal layer form flattened crosses or horizontal tubes rather than six pointed stars as proposed by Gross (1956). There are additional differences between our scan data and the 3D model proposed by Gross (1956), however, these may result from idealistic simplification which he himself mentions. 3D data has therefore improved our understanding of canal geometry mostly in terms of canal texture and the canal geometry of the lower middle layer.

5.2 | The topological differentiation of the vertebrate dermal skeleton

Extant osteichthyans show extensive differentiation across the dermal skeleton. The cranial dermal bones often exhibit a tripartite structure, with compact superficial and basal bone and a cancellous middle layer (de Buffrenil et al., 2016). By contrast, the trunk dermal skeleton is fundamentally distinct, and is variously modified into elasmoid scales, ganoid scales and cosmoid scales, is histologically distinct, or entirely absent (Lu et al., 2016; Sire et al., 2009). Despite this, the cranial and trunk dermal skeletons often share phylogenetically derived features, presumably reflecting common developmental mechanisms and a shared ancestry (e.g. cosmine occurs both on the cranium and scales of extinct sarcopterygians; Thomson, 1977). A prime example of differentiation within the trunk dermal skeleton is seen in the transition from scales to lepidotrichia which share a common histology in early actinopterygians such as *Cheirolepis*, but diverge significantly in extant taxa (Zylberberg et al., 2015).

Tremataspis mammillata represents an early stage in dermal skeletal differentiation across the trunk and cranium, with reduction of the middle layer posteriorly until it is almost absent in the caudal scales. A similar level of skeletal differentiation is seen in heterostracans, where the middle layer is well developed in the headshield, but reduced or absent in the trunk scales (Keating et al., 2015). In *Tremataspis*, this is associated with a reduction in differentiation between the lower mesh canals and the superficial + lower canal networks. The vascular geometry of odontodes is a product of odontode growth (Donoghue, 2002) and constraint of canal growth by scale geometry is evident where mesh canals and the superficial canal network extend straight to the margins of the scale. In addition, the mesh canals of the trunk scales form only 1 row of polygons parallel to the scale long axis. In the smallest caudal scales no polygons can form at all. Differentiation is also seen in the external ornamentation of numerous thyestiidan genera, which show a continuous change from the headshield to the scales (Märss et al., 2015). Within the headshield of *Tremataspis*, there is variation

in relative layer thickness across the headshield, especially in terms of the basal layer. The superficial layer also becomes especially thickened near the posterior angle, however, compared to some other osteostracans its cranial histology is relatively homogeneous. The derived zenaspidian *Superciliaspis* shows extensive variation in external ornamentation within the headshield (Hawthorn et al., 2008) and *Dartmuthia* shows strong differentiation in the histology of the dorsal and ventral headshield (Denison, 1951).

5.3 | Homologies of dermal skeletal tissue in *Trememataspis mammilata*

The presence of partially polarised and embedded lacunae with multiple processes in the superficial layer is consistent with the definition of mesodentine (Ørvig, 1967). The boundary between the dentine and hypermineralised cap is irregular and crossed by dentine canaliculi identifying it as bitypic enameloid (Kawasaki and Weiss, 2008). The polarisation of dentine canaliculi away from the superficial canal network as well as the concentrically arranged dentine lamellae which encompass the lacunae and canals (la1-la3 in *Trememataspis*) demonstrates progressive retreat of the odontocytes towards these canals, confirming their nature as pulp cavities (Smith and Sansom, 2000). Pulp cavities receive both blood vessels and nerves, and the dendritic configuration of the lower canal network supports their interpretation as vascular structures. In addition, the position of this network within the middle layer and beneath a superficial canal network which supplies the dentine lacunae supports their homology with the radiating canals of other osteostracans (Denison, 1947; Wängsjö, 1946). Currently, dentine is known to derive exclusively from neural crest (Hall, 2015), but is absent gtom the scales of teleosts. Traditionally, trunk neural crest has been the prime candidate for the mesenchyme forming the trunk dermal skeleton (Smith and Hall, 1993), however, recent labelling studies have revealed a mesodermal origin for the trunk dermal skeleton of teleosts (Lee et al., 2013; Mongera and Nusslein-Volhard, 2013). The presence of dentine on the dermal skeletons of numerous total group gnathostomes suggests that, ancestrally, the trunk dermal skeleton received neural crest contributions. Some support for this is found in cell lineage labelling of trunk neural crest cells contributing to the developing placoid scales in skate embryos (Gillis et al., 2017). There is no evidence to support the alternative interpretation, that mesoderm was ancestrally capable of forming odontoblasts.

The middle layer contains lenticular lacunae with radiating canaliculi which are consistent in diameter (long axis 14µm in *Trememataspis*, approx. 13µm in mouse; 9-15 µm in *Lampris*) and shape with osteocytes (Davesne et al., 2019; Vatsa et al., 2008) identifying the tissue as bone and the concentric structures as primary osteons. The truncation of lamellae where the lower mesh canals

connect to the lower canal network most likely result from resorption around the vascular canals (Francillon-Vieillot et al., 1990). The continuity of the sieve plates in *Trememataspis* with the lamellae surrounding the lower mesh canals suggests that they consist of bone and were deposited centripetally.

Conflicting interpretations over the nature of the basal layer in osteostracans (isopedin, elasmodine and ossification of the stratum compactum) (Sire et al., 2009) distil down to distinguishing between structural definitions and developmental origins (osteogenic, odontogenic or metaplastic). The elasmodine of actinopterygians is thought to be odontogenic (Sire and Huysseune, 2003) and can therefore be described as odontogenic poorly mineralised isopedin, however, its odontogenic/osteogenic origin in sarcopterygians has yet to be tested. Elasmodine in *Polypterus* occurs between overlying dentine and underlying bone. Sire *et al.* (2003) suggest that the morphology, topological relations and growth of basal tissue in *Trememataspis* is consistent with *Polypterus* elasmodine, proposing that the two tissues are homologous. However, the identification of bone separating the basal layer from the overlying dentine in *Trememataspis* is inconsistent with *Polypterus* elasmodine. Moreover, the phylogenetic distribution of odontogenic elasmodine is uncertain. Sire *et al.* (2003) suggest that the elasmodine of coelacanths and dipnoans is homologous to that in actinopterygians making these layers odontogenic. A prediction of their hypothesis is the occurrence of a distinct elasmodine layer above the osteogenic tissues in the osteichthyan common ancestor and all of the cosmoid and rhomboid taxa bridging the phylogenetic gap between extant actinopterygians and sarcopterygians, however they acknowledge that the fossil record has not confirmed this prediction (Sire and Huysseune, 2003). The mineralised isopedin of extinct sarcopterygians (Gross, 1956; Mondéjar-Fernández and Clement, 2012; Qu et al., 2013) has a similar structure to the poorly mineralised elasmodine in extant sarcopterygian scales (e.g. Kemp et al., 2015; Smith et al., 1972) and could therefore be osteogenic and nonhomologous to teleost elasmodine. This negates the assumption of a distinct elasmodine layer in basal osteichthyans. As a result, the expected presence of odontogenic elasmodine in the basal layer of the osteichthyan and gnathostome common ancestors cannot be corroborated.

Metaplastic ossification results from the direct conversion of preformed tissue into bone. It is distinct from intramembranous ossification in which dermal elements derive from a discrete condensation (Vickaryous and Sire, 2009). The basal layer of *Trememataspis* shares many features with the stratum compactum of the vertebrate dermis, these include: the angle between overlapping fibre bundles (approx. 70^{o} in *Trememataspis*, 50-70 ^{o} in sharks), fibre bundles which alternate between the same two orientations in successive lamellae, and basally increasing fibre bundle thickness (Motta, 1977).

Despite these observations, some of the scales in *Trematapsis* are more consistent with development from condensation. As in extant osteichthyans, the lamellae of the basal layer in the larger trunk scales curve according to the scale margins rather than following the contour of the body surface as seen in the stratum compactum (Long et al., 1996). Moreover, the absence of vertical collagen fibrils characteristic of the dermis (Le Guellec et al., 2004) is inconsistent with metaplasia of preformed dermal tissue. The ambiguity surrounding the ancestral status of elasmodine combined with development from a condensation allows us to identify the basal tissue of *Trematapsis* as osteogenic isopedin.

The similarity of the *Trematapsis* basal layer to stratum compactum most likely reflects the fact that the dermal skeleton is a differentiation of the vertebrate dermis (Moss 1972). For example, scale development in zebrafish represents a continuation of dermal development, with the fibroblasts forming the elasmodine of the scales deriving from a population which contributes to the stratum compactum (Le Guellec et al., 2004). Curiously the stratum compactum of zebrafish (Le Guellec et al., 2004) is in some respects more similar to the elasmodine of its scales (Sire and Akimenko, 2004) than to the stratum compactum of non-teleosts, with each successive lamella consisting of multiple layers of nanometre scale collagen fibrils rather than distinct micrometre scale fibre bundles. Therefore, shared primitive traits found in unmineralised dermal tissue can determine the structure of the isopedin which derives from it. Similarly, the great resemblance between the superficial layer of *Trematapsis* and galeaspids to the stratum compactum (Wang et al., 2005) is suggestive of poor differentiation of the basal layer from the surrounding dermal tissue, which is perhaps generally representative of stem-gnathostomes immediately prior to the origin of jawed vertebrates.

The large cavities in the basal layer of *Trematapsis* are often interpreted as resorption phenomena (Denison, 1952; Gross, 1956). However in mineralising osteichthyan basal tissues the fibre bundles project ahead of the mineralisation front just as in *Trematapsis* (Meunier, 1981) so these features could represent growth rather than resorption (Denison, 1947). It may be possible to test this by searching for oblate Mandl's corpuscles which result from mineralisation of collagen fibrils in the elasmodine of osteichthyans (Meunier, 1981). The cavities must have contained vasculature since they lead into large ramifying canals in the middle layer. The smaller spaces in the basal layer show no evidence of cell like morphology and extend along surrounding fibre bundles for lengths far exceeding those of typical osteocytes. Therefore these "lacunae" are interpreted as spaces resulting from closely packed cylinders (Wang et al., 2005).

5.4 | Growth in *Trematapsis*

Based on different developmental stages in *Trematapsis* and the lack of evidence for extensive resorption in many osteostracans, Denison (1947; 1952) inferred that the headshield mineralised in a single event with centripetal addition of matrix in a superficial to basal direction, leading to the conclusion that growth was determinate and unipolar sensu Afanassieva (2014). The concentric arrangements of superficial and middle layer lamellae described above (4.4.2 | Dorsal trunk scales) suggest centripetal deposition of matrix towards the superficial and lower vascular networks and centrifugal deposition away from the mesh canals. This began with la3 enameloid, followed by la2 dentine and bone surrounding the polarised lacunae and upper mesh canals and finally la1 dentine and bone lining the polarised lacunae and middle layer vasculature. la1 is also deposited centripetally in the lower mesh canals. Apparent truncation of lamellae indicates that some resorption occurred prior to the deposition of la1 which has a distinct boundary. That these lamellae form a continuous surface through the scales (Fig. 10) suggests that they represent lines of arrested growth. Importantly, these concentric zones correspond to the growth stages of Denison (1947). This mode of development explains the difference in texture between the upper and lower mesh canals. The centripetal addition of tissue towards the lower mesh canals and superficial and lower canal networks caused cell lacunae to open onto the canal surfaces producing a rough texture. The centrifugal addition of enameloid, dentine and bone away from the upper mesh canals resulted in a smooth texture.

Determinate growth is supported by size data analysed by Denison (1952), who found that the coefficients of variation seen in *Trematapsis mammilata* and many other osteostracans, were consistent with those for samples of mammals at the same age. However, several zenaspidians seem to have been capable of growth post-mineralisation. An ontogenetic series of the derived zenaspidan *Superciliaspis* demonstrates that growth could occur by addition and fusion of tesserae along with marginal growth of individual tesserae as suggested by the concentric pattern of odontodes in each tessera (Hawthorn et al., 2008). Odontode patterning in the zenaspid *Diademaspis* and an indeterminate cornuate corroborate the hypothesis of marginal growth (Keating et al., 2012). In addition, juvenile growth stages of *Parameteoraspis* show that tesserae were initially separate and subsequently fused on reaching maximum size (Janvier, 1985a). Bipolar growth (Afanassieva, 2014) has been found in the thyestiidans *Procephalaspis* (Janvier, 1996; Ørvig, 1951) and *Trematapsis milleri* (Märss et al., 2015) which show superposition of odontodes. A collection of thyestiid fragments described by Gross (1961) and later named *Tahulaspis* (Märss et al., 2015) show initial ontogenetic stages with ridge like tubercles of primary dentine and grooves between them containing sieve plates. Subsequently, secondary dentine was added over the grooves creating a smooth superficial layer, as in *Trematapsis*, which enclosed a mesh canal system between the

primary dentine ridges. This indicates that the mesh canal system was present in the dermis between a primary generation of odontodes and interacted with them during development (common patterning between the two). Secondly, it shows that there were two ways of generating a continuous superficial layer in osteostracans. In *Trematapsis* there is no evidence for primary odontodes or extensive remodelling, so the mesh canals must have been embedded within a single phase of mineralisation. In *Tahulaspis*, the smooth superficial surface was achieved by filling in gaps between the tubercles. Similar secondary superficial tissue with mesh canal pores has been found on the headshield of *Trematapsis milleri* (Märss et al., 2015). This demonstrates that unlike *T. mammilata*, some thyestidians were capable of increasing the thickness of the dermal skeleton superficially and suggests that *Trematapsis* growth is not representative of the general thyestidian condition. Based on the pattern of tubercles and radiating canals, *Thyestes* has been suggested to have engaged in marginal growth of unfused tesserae and then fusion at adulthood with addition of odontodes around tubercles at the polygonal centres (Afanassieva, 2014). Marginal growth of tesserae almost certainly occurred in the derived zenaspidians which show separate tesserae and ontogenetic stages (Hawthorn et al., 2008), however the only evidence for marginal growth in forms with consolidated headshields is the polygonal patterning of dermal skeletal freatures and concentric patterns of odontodes. Detailed histological examination of tessellate osteostracans will be needed to verify whether some forms with a basally continuous headshield at adulthood could grow by expanding the tesserae.

5.5 | The mesh canals of *Trematapsis*, implications for growth and patterning of the dermal skeleton

Gross (1956) and Thomson (1977) highlighted the similarity between the mesh canals of *Trematapsis* and the pore canal system in extinct sarcopterygians. A pore canal system is plesiomorphic for osteichthyans (Lu et al., 2016), and similar canal systems appear in acanthodians (Gross, 1956) and heterostracans ("intermediate canals"). The homology of these structures among early vertebrates remains unresolved; equally mysterious is their function. Such structures are often interpreted as sensory due to their continuity with the lateral line system and regular geometric arrangement (Denison, 1947; Gross, 1956; Qu et al., 2015; Thomson, 1977). The ancestral condition of the vertebrate sensory system is thought to consist of mechanosensory neuromasts and electrosensory ampullae, although the latter have been lost and regained multiple times (Gibbs, 2004). Canals containing neuromasts in extant taxa range from 100-7000µm in diameter (Gibbs, 2004), whereas the mesh canals of *Trematapsis* are far smaller at only 30-40µm wide. More consistency is found between the pore cavities of *Trematapsis* and flask-shaped electrosensetive ampullae (e.g. 80µm in the siluriform *Kryptopterus* and 700µm in the elasmobranch *Scylliorhinus* vs approx. 110µm in

Trematapsis) and the sieve plate perforations are similar in size to the hair cells lining the ampulla base (measurements taken from figures in Jørgensen, 2005). However, the pore cavities of extinct dipnoans occur alongside unambiguous ampullary cavities making them nonhomologous by conjunction. An alternative (though not necessarily mutually exclusive) interpretation is that these are vascular structures which, representing the only connection between the underlying dermal vasculature and the surface of the cranial dermal bones, may have been necessary to supply overlying epidermal tissue (Bemis and Northcutt, 1992). Indeed, there is no other plausible means by which vascular could have arisen to the superficial epidermis.

Function aside, patterning of vascular canal systems and nerves associated with odontodes are a product of odontode growth (Donoghue, 2002). The presence of enameloid in the pore cavities of *Trematapsis* and the occurrence of the sieve plates on the surface of the dermal skeleton in other thyestiids supports the notion that the upper mesh canals represent a point of ectodermal contact (Qu et al., 2015), suggesting that they represent partial boundaries between regions of odontogenesis. Reif (1982) proposed a simple reaction-diffusion system in which odontodes are patterned by mutual inhibition of dermal papillae. This model has subsequently been used to accurately reproduce odontode patterning (Maisey and Denton, 2016). Donoghue (2002) considered the factors likely implicated in regulating this reaction-diffusion system which has now been effectively validated in the development of shark scale by Cooper et al. (Cooper et al., 2018). Reaction-diffusion mechanics are thought to underlie pattern formation in numerous living organisms from cyanobacterial chains to the arrangement of feather buds in birds (Economou and Green, 2014). Hexagonal packing as seen in osteostracan mesh canals and labyrinthine patterns formed by odontodes in heterostracans (which are bounded by mesh-canal like structures) can both be generated in models of morphogenetic Turing patterns (Facchini and Mocenni, 2013). Therefore, the patterning of the mesh canals can be explained by the growth of mutually inhibiting dermal papillae, which constrain the growth of canals supplying the overlying epidermis/dermis.

Within this framework, the so-called “growth-lines” of *Trematapsis mammilata* (Denison, 1947) are especially interesting, as they demonstrate a failure of the pattern-forming mechanism consistent with the reaction-diffusion hypothesis and show a link in skeletal patterning which encompasses the skeletogenic and odontogenic components. These represent abnormalities, occurring in a small proportion of specimens. According to Denison’s (1947) growth hypothesis, the mesh canals were sensory and embedded within the dermis prior to mineralisation. Focussing on the “growth lines” representing regions where the mesh canals form a labyrinthine rather than polygonal mesh, Denison suggested that these elongate mesh canal polygons resulted from stretching of the

integument and attendant mesh canals during growth combined with failure of the mesh canals to form secondary polygons within the expanded integument. However, there is no evidence that the mesh canals existed prior to growth of the dermal skeleton. If it is assumed that they result from skeletal growth then the "growth lines" must result from pattern breakdown during odontogenesis. The elongate mesh canal networks within the "growth lines" resemble the labyrinthine Turing pattern (Facchini and Mocenni, 2013), so it is likely a consequence of local effects altering a more general spatial reaction-diffusion system. Moreover, when these regions pass through the sensory fields the tesserae are undifferentiated (Denison, 1947). The sensory field tesserae incorporate all three layers of the dermal skeleton. Therefore, these growth defects demonstrate a common patterning mechanism linking the odontogenic and skeletogenic systems of the osteostracan dermal skeleton (Donoghue, 2002).

5.6 | Is *Trematapsis* representative of the ancestral osteostracan condition?

Trematapsis is generally accepted as a highly derived osteostracan, lacking pectoral appendages, cornuae and having two pairs of lateral sensory fields (Janvier, 1984; Sansom, 2008; 2009). Moreover, its histology is unusual for osteostracans. The irregular lower vascular network lacks a radiating pattern and a continuous superficial layer encloses the mesh canals. In many early diverging osteostracans, including *Ateleaspis* (Afanassieva 1999), *Hemicyclaspis*, and many zenaspidans (Stensiö, 1927; 1932), the superficial and middle layers are divided into polygonal tessarae by so-called inter-areal canals, between which finer intra-areal canals extended, together comprising the "mesh canal" system (sensu Gross, 1961). Given that this tessellate condition is so prevalent among osteostracans, it is likely plesiomorphic for the clade. In some derived zenaspidians such as *Escuminaspis* (Ørvig, 1968) and *Superciliaspis* (Hawthorn et al., 2008), the tesserae are entirely separate. The presence of truly radiating canals in *Ateleaspis* (Afanassieva, 1999), *Hemicyclaspis* and numerous cornuate taxa (Stensiö, 1932) suggests that they were also plesiomorphic within Osteostraci and the more disorganised condition in *Trematapsis* is derived.

Most thyestiidans lack a continuous superficial layer instead having an arrangement of tubercles and traces of polygonal subdivision; mesh canals are underlain by sieve plates exposed as grooves on the superficial surface in *Thyestes*, *Saaremaaspis*, *Witaaspis*, *Oeselaspis* (Denison, 1951; Gross, 1968b; Märss et al., 2015), and the early-branching genus *Procephalaspis* (Sansom, 2008). *Dartmuthia* has a combination of tesserae and tubercles on the dorsal headshield, whereas the ventral headshield is similar to that of *Trematapsis*, but the mesh canals communicate with the surface via grooves rather than pores, such that the sieve plates are deeply invaginated (Denison, 1951; Gross, 1968a). *Sclerodus* is unusual in lacking a clear superficial layer (Denison, 1951). Therefore, a dermal skeleton

with a tuberculated surface in which the mesh canals are exposed and radiating canals occur beneath polygonal centres seems to be plesiomorphic for thyestiidans.

Despite these stark differences, within the broad sense of tissue types and layers the dermal skeleton of *Trematapis* can be used to represent osteostracans in general. The three-layered condition of *Trematapis* is shared with almost all osteostracans (Sire et al., 2009), with a superficial layer of dentine and enameloid, a middle layer of cellular bone and a basal layer of lamellar isopedin. Mesodentine seems universal within thyestiidans (Märss et al., 2015) and probably osteostracans in general (e.g. Ørvig, 1951; 1967). Despite this, the polarity of the dentine tubules varies within a single taxon (e.g. compare the tubercles to the smooth regions of *T. mammilata*; Fig. 4A vs Fig. 9B) and between taxa, for example there is strong polarity in dentine tubules of *Ateleaspis* (text-fig 11a in Ørvig, 1951). However, comparable systematic analyses of the diversity of osteostracans are required to test the general relevance of *Trematapis* as a model for the dermal skeleton within this clade and, indeed, for the nature of the dermal skeleton in the ancestor of jawed vertebrates.

5.7 | Descriptions *versus* hypotheses in palaeohistology

The development and application of X-Ray based microtomographic methods has led to a revolution in palaeontology, revealing palaeobiological data otherwise hidden due to the rarity of fossil material and the destructive nature of traditional tomographic methods (Cunningham et al., 2014b). Palaeohistologists, in particular, have wrestled with attempting to infer the three-dimensional structure of histological tissues and their cellular and vascular spaces, from essentially two-dimensional thin sections through skeletal remains. They achieved this by developing three-dimensional reconstructions that integrate the perspective provided by orthogonal and oblique sections through the same materials. Denison (1947), Wangsjö (1952), Gross (1956; 1961), and Karatajute-Talimaa (1995; 1998) have been among the most effective in developing such models, and Denison's model of the dermal skeleton in *Trematapis mammillata* is among the most detailed and widely known example (Denison, 1947). Qu et al. (2015) call this entire approach into question based principally on the differences they observe between their tomographic description of the dermal skeleton in *Trematapis schmidti*, based on a partial microtomographic scan of a scale, and the three-dimensional model of the histological structure of the cephalothoracic headshield of *Trematapis mammillata*. These differences are explained in part by the fact that Qu et al. (2015) studied material from a different species and from a topological distinct portion of the skeleton than that explained by Denison's histological model. More importantly, Qu et al. (2015) miss the point that Denison's model is an attempt not simply to reconstruct the three-dimensional histological structure of the cephalothoracic headshield of *Trematapis mammillata*, which he sampled with his histological

sections, but also to rationalise the variation that he observed. Thus, Denison's model, like all of the hand-drawn histological reconstructions that Qu et al. (2015) dismiss, is a scientific hypothesis that can be tested, but cannot be superseded by the three-dimensional computed tomographic descriptions of histological structure that Qu et al. (2015) present. Digital modelling techniques provide a means of integrating such evidence into more holistic scientific hypotheses that may supplement and ultimately replace traditional hand-drafting (e.g. Cunningham et al., 2014a; Lautenschlager, 2016) but, in the interim, Denison's model of the histological structure of the cephalothoracic dermal headshield remains the most holistic interpretation of the available data from optical thin sections, SEM ground sections, and synchrotron microtomography.

6 | CONCLUSIONS

Osteostracans capture a pivotal stage in the assembly of the gnathostome dermal skeleton, representing the earliest appearance of a true tripartite structure with cellular osteons. The 3D model provided by Denison (1947) is largely confirmed and the scans reveal that some histological differentiation between the headshield and trunk occurred in osteostracans. They also hint at the wealth of 3D data remaining to be discovered on the evolution of topological differentiation across the dermal skeletons of almost all major groups of early mineralising vertebrates. Finally, within the current phylogenetic framework (Sansom, 2008) *Trematapis* is highly derived and exhibits an unusual histology. Moreover ontogenetic series demonstrate that some osteostracans were capable of growth post-mineralisation (Hawthorn et al., 2008) potentially making *Trematapis* unrepresentative of the ancestral osteostracan condition. Therefore, a wide variety of osteostracan taxa must be surveyed within a phylogenetic context in order to fully understand their significance in the evolutionary assembly of the gnathostome skeleton.

ACKNOWLEDGEMENTS

This research study was conducted by James O'Shea in partial fulfilment of the MSci Palaeontology and Evolution at the School of Earth Sciences, University of Bristol, working under the guidance of Joseph Keating and Philip Donoghue. James was one of the most gifted undergraduate students that we have had the pleasure of supervising, clearly destined to become a leading light in which ever field of research he chose to focus upon. His untimely death is a great loss to our science, as well as incalculable personal tragedy for all who knew him. James would have wished to acknowledge the love, support, help and friendship of his family, as well as his friends and colleagues in Bristol Palaeobiology, all of whom miss him dearly. The research leading to these results received funding

from the European Union's Horizon 2020 research and innovation programme under grant agreement n.°730872, project CALIPSOplus. We also acknowledge the Paul Scherrer Institut, Villigen, Switzerland for provision of synchrotron radiation beamtime at the TOMCAT beamline X02DA of the Swiss Light Source and we would like to thank Dr Federica Marone for assistance. PCJD was funded by NERC NE/G016623/1.

CONFLICT OF INTEREST

The authors have no conflict of interest.

ORCID

Joseph N. Keating https://orcid.org/0000-0002-2667-7795

Philip C. J. Donoghue https://orcid.org/0000-0003-3116-7463

REFERENCES

Afanassieva OB. 1999. The exoskeleton of *Ungulaspis* and *Ateleaspis* (Osteostraci, Agnatha) from the Lower Devonian of Severnaya Zemlya, Russia. Acta Geologica Polonica 49:119-123.

Afanassieva OB. 2014. Development of the exoskeleton in osteostracans: new evidence of growth. Paleontological Journal 48:973-979.

Bemis WE, Northcutt RG. 1992. Skin and blood vessels of the snout of the Australian lungfish, *Neoceratodus forsteri*, and their significance for interpreting the cosmine of Devonian lungfishes. Acta Zoologica (Stockholm) 73(2):115-139.

Bölau E. 1951. Das sinnesliniensystem der trematapiden und dessen beziehungen zu anderen gefässsystemen des exoskeletts. Acta Zoologica (Stockholm) 32:31-40.

Cooper RL, Thiery AP, Fletcher AG, Delbarre DJ, Rasch LJ, Fraser GJ. 2018. An ancient Turing-like patterning mechanism regulates skin denticle development in sharks. Science Advances 4:1-10.

Cunningham JA, Rahman IA, Lautenschlager S, Rayfield EJ, Donoghue PC. 2014a. A virtual world of paleontology. Trends in ecology & evolution 29(6):347–357.

Cunningham JE, Donoghue PCJ, Bengtson S. 2014b. Distinguishing biology from geology in soft tissue preservation. Paleontological Society Special Publication 20:275-288.

Davesne D, Meunier FJ, Schmitt AD, Friedman M, Otero O, Benson RBJ. 2019. The phylogenetic origin and evolution of acellular bone in teleost fishes: insights into osteocyte function in bone metabolism. Biological reviews of the Cambridge Philosophical Society.

de Buffrenil V, Clarac F, Canoville A, Laurin M. 2016. Comparative data on the differentiation and growth of bone ornamentation in gnathostomes (Chordata: Vertebrata). Journal of Morphology 277:634-670.

Denison RH. 1947. The exoskeleton of *Trematapsis*. American Journal of Science 245:337-365.

Denison RH. 1951. The exoskeleton of early Osteostraci. Fieldiana Geology 11(4):199-218.

Denison RH. 1952. Early Devonian fishes from Utah: Part I. Osteostraci. Fieldiana Geology 11(6):265-287.

Denison RH. 1963. The early history of the vertebrate calcified skeleton. Clinical Orthopaedics and Related Research 31:141-152.

Donoghue PCJ. 2002. Evolution of development of vertebrate teeth and scales: unravelling concepts, regulatory theories and homologies. Paleobiology 28(4):474-507.

Donoghue PCJ, Keating JN, Smith A. 2014. Early vertebrate evolution. Palaeontology 57(5):879-893.

Donoghue PCJ, Purnell MA. 2005. Genome duplication, extinction and vertebrate evolution. Trends in ecology & evolution 20(6):312-319.

Donoghue PCJ, Sansom IJ. 2002. Origin and early evolution of vertebrate skeletonization. Microscopy Research & Technique 59(5):352-372.

Donoghue PCJ, Sansom IJ, Downs JP. 2006. Early evolution of vertebrate skeletal tissues and cellular interactions, and the canalization of skeletal development. Journal of Experimental Zoology - Part B: Molecular and Developmental Evolution 306B:278-294.

Economou AD, Green JBA. 2014. Modelling from the experimental developmental biologists viewpoint. Seminars in Cell and Developmental Biology 35:58-65.

Facchini A, Mocenni C. 2013. Recurrence methods for the identification of morphogenetic patterns. PLoS One 8:e73686.

Francillon-Vieillot H, de Buffrénil V, Castanet J, Géraudie J, Meunier FJ, Sire J-Y, Zylberberg L, Ricqlès Ad. 1990. Microstructure and mineralization of vertebrate skeletal tissues. In: Carter JG, editor. Skeletal biomineralization: patterns, processes and evolutionary trends. New York: Van Nostrand Reinhold. p 471-530.

Gibbs MA. 2004. Lateral line receptors: where do they come from developmentally and where is our research going? Brain, Behavior and Evolution 64:163-181.

Giles S, Rücklin M, Donoghue PCJ. 2013. Histology of "placoderm" dermal skeletons: Implications for the nature of the ancestral gnathostome. Journal of Morphology 274:627-644.

Gillis JA, Alsema EC, Criswell KE. 2017. Trunk neural crest origin of dermal denticles in a cartilaginous fish. Proceedings of the National Academy of Sciences of the United States of America 114(50):13200-13205.

Gillis JA, Donoghue PCJ. 2007. The homology and phylogeny of chondrichthyan tooth enameloid. Journal of Morphology 268:33-49.

Gross W. 1935. Histologische Studien am Aussenskelett fossiler Agnathen und Fische. Palaeontographica (Abt A) 83:1-60.

Gross W. 1956. Über Crossopterygier und Dipnoer aus dem baltischen Oberdevon im Zusammenhang einer vergleichenden Untersuchung des Porenkanalsystems paläozoischer Agnathen und Fische. Kungliga Svenska Vetenskapsakademiens Handlingar 5(6):1-140.

Gross W. 1961. Aufbau des Panzers obersilurischer Heterostraci und Osteostraci Norddeutschlands (Geschiebe) und Oesels. Acta Zoologica (Stockholm) 42(1-2):73-150.

Gross W. 1968a. Beobachtungen mit dem Elektronenraster-Auflichtmikroskop an den Siebplatten und dem Isopedin von *Dartmuthia* (Osteostraci). Paläontologische Zeitschrift 42(1/2):73-82.

Gross W. 1968b. Die agnathen-fauna der Silurischen Halla-schichten Gotlands. Geologiska Föreningens i Stockholm Förhandlingar 90:369-400.

Hall BK. 2014. Endoskeleton/Exo (dermal) skeleton - mesoderm/neural crest: two pairs of problems and a shifting paradigm. Journal of Applied Ichthyology 30:608-615.

Hall BK. 2015. Bones and cartilage: developmental and evolutionary skeletal biology. Amsterdam: Elsevier. 892 p.

Hawthorn JR, Wilson MVH, Falkenberg AB. 2008. Development of the dermoskeleton in *Superciliaspis gabrielsei* (Agnatha: Osteostraci). Journal of Vertebrate Paleontology 28(4):951-960.

Janvier P. 1984. The relationships of the Osteostraci and the Galeaspida. Journal of Vertebrate Paleontology 4:344-358.

Janvier P. 1985a. Les Céphalaspides du Spitsberg: anatomie, phylogénie et systématique des Ostéostracés siluro-devoniens; révisions des Ostéostracés de la Formation de Wood Bay (Dévonien inférieur du Spitsberg). Paris: CNRS édition. 244 p.

Janvier P. 1985b. Les thyestidiens (Osteostraci) du Silurien de Saaremaa (Estonie). Deuxieme partie: analyse phylogénétique, répartition stratigraphique, remarques sur les genres *Auchenaspis, Timanaspis, Tyriaspis, Didymaspis, Sclerodus* et *Tannuaspis*. Annales de Paléontologie 71(3):187-216.

Janvier P. 1996. Early Vertebrates. Oxford: Oxford University Press. 393 p.

Janvier P. 2004. Calcified cartilage in the paired fins of the osteostracan *Escuminaspis laticeps* (Traquair 1880), from the Late Devonian of Miguasha (Québec, Canada), with a consideration of the early evolution of the pectoral fin endoskeleton in vertebrates. Journal of Vertebrate Paleontology 24:773-779.

Jeppsson L, Anehus R, Fredholm D. 1999. The optimal acetate buffered acetic acid technique for extracting phosphatic fossils. Journal of Paleontology 73(5):964-972.

Jørgensen JM. 2005. Morphology of electroreceptive sensory organs. In: Bullock TH, Hopkins CD, Popper AN, Fay RR, editors. Electroreception. New York: Springer. p 47-67.

Karatajuté-Talimaa V. 1995. The Mongolepidida: scale structure and systematic position. Geobios 19 supplement:35-37.

Karatajuté-Talimaa V. 1998. Determination methods for the exoskeletal remains of early vertebrates. Mitteilungen aus dem Museum für Naturkunde in Berlin, Geowissenschaftliche Reihe 1:21-52.

Kawasaki K, Weiss KM. 2008. SCPP gene evolution and the dental mineralization continuum. J Dent Res 87(6):520-531.

Keating JN, Donoghue PCJ. 2016. Histology and affinity of anaspids, and the early evolution of the vertebrate dermal skeleton. Proceedings of the Royal Society B: Biological Sciences 283:20152917.

Keating JN, Marquart CL, Donoghue PCJ. 2015. Histology of the heterostracan dermal skeleton: Insight into the origin of the vertebrate mineralised skeleton. Journal of Morphology 276:657–680.

Keating JN, Marquart CL, Marone F, Donoghue PCJ. 2018. The nature of aspidin and the evolutionary origin of bone. Nat Ecol Evol 2:1501-1506.

Keating JN, Sansom RS, Purnell MA. 2012. A new osteostracan fauna from the Devonian of the Welsh Borderlands and observations on the taxonomy and growth of Osteostraci. Journal of Vertebrate Paleontology 32:1002-1017.

Kemp A, Heaslop M, Carr A. 2015. Scale structure in the Australian lungfish, Neoceratodus forsteri (Osteichthyes: Dipnoi). J Morphol 276(10):1137-1145.

Lautenschlager S. 2016. Reconstructing the past: methods and techniques for the digital restoration of fossils. R Soc Open Sci 3(10):160342.

Le Guellec D, Morvan-Dubois G, Sire J-Y. 2004. Skin development in bony fish with particular emphasis on collagen deposition in the dermis of the zebrafish (*Danio rerio*). International Journal of Developmental Biology 48:217-231.

Lee RT, Thiery JP, Carney TJ. 2013. Dermal fin rays and scales derive from mesoderm, not neural crest. Current biology : CB 23(9):R336-337.

Long JH, Hale ME, McHenry MJ, Westneat MW. 1996. Functions of fish skin: flexural stiffness and steady swimming of longnose gar *Lepisosteus osseus* Journal of Experimental Biology 199:2139-2151.

Lu J, Giles S, Friedman M, den Blaauwen JL, Zhu M. 2016. The oldest actinopterygian highlights the cryptic early history of the hyperdiverse ray-finned fishes. Current Biology.

Maisey JG, Denton JSS. 2016. Dermal denticle patterning in the Cretaceous hybodont sharkTribodus limae(Euselachii, Hybodontiformes), and its implications for the evolution of patterning in the chondrichthyan dermal skeleton. Journal of Vertebrate Paleontology:e1179200.

Marone F, Stampanoni M. 2012. Regridding reconstruction algorithm for real time tomographic imaging. Journal of Synchrotron Radiation 19:1-9.

Märss T, Afanassieva O, Blom H. 2015. Biodiversity of the Silurian osteostracans of the East Baltic. Earth and Environmental Science Transactions of the Royal Society of Edinburgh 105(02):73-148.

Meunier FJ. 1981. 'Twisted plywood' structure and mineralization in the scales of a primitive living fish, *Amia calva*. Tissue & Cell 13:165-171.

Mondéjar-Fernández J, Clement G. 2012. Squamation and scale microstructure evolution in the Porolepiformes Sarcopterygii Dipnomorpha based on *Heimenia ensis* from the Devonian of Spitsbergen. Journal of Vertebrate Paleontology 32:267-284.

Mongera A, Nusslein-Volhard C. 2013. Scales of fish arise from mesoderm. Current biology : CB 23(9):R338-339.

Motta PJ. 1977. Anatomy and functioanl morphology of dermal collagen fibers in sharks. Copeia 1977:454-464.

Ørvig T. 1951. Histologic studies of ostracoderms, placoderms and fossil elasmobranchs 1. The endoskeleton, with remarks on the hard tissues of lower vertebrates in general. Arkiv för Zoologi 2(2):321-454.

Ørvig T. 1967. Phylogeny of tooth tissues: evolution of some calcified tissues in early vertebrates. In: Miles AEW, editor. Structural and Chemical Organisation of Teeth. New York and London: Academic Press. p 45-110.

Ørvig T. 1968. The dermal skeleton: General considerations. In: Ørvig T, editor. Current Problems of Lower Vertebrate Phylogeny. Stockholm: Almquist & Wiksell. p 374-397.

Ørvig T. 1977. A survey of odontodes ('dermal teeth') from developmental, structural, functional, and phyletic points of view. In: Andrews SM, Miles RS, Walker AD, editors. Problems in vertebrate evolution: Linnean Society Symposium Series 4. p 53-75.

Patten W. 1912. The evolution of vertebrates and their kin. Philadelphia: P. Blakinson’s Son and Co.

Qu Q, Blom H, Sanchez S, Ahlberg P. 2015. Three-dimensional virtual histology of Silurian osteostracan scales revealed by synchrotron radiation microtomography. J Morphol 276(8):873-888.

Qu Q, Zhu M, Wang W. 2013. Scales and dermal skeletal histology of an early bony fish Psarolepis romeri and their bearing on the evolution of rhombic scales and hard tissues. PLoS One 8(4):e61485.

Reif W-E. 1982. Evolution of dermal skeleton and dentition in vertebrates: The odontode regulation theory. Evolutionary Biology 15:287-368.

Sansom RS. 2008. The origin and early evolution of the Osteostraci (Vertebrata): A phylogeny for the Thyestiida. Journal of Systematic Palaeontology 6(3):317-332.

Sansom RS. 2009. Phylogeny, classification and character polarity of the Osteostraci (Vertebrata). Journal of Systematic Palaeontology 7(1):95-115.

Sire J-Y, Akimenko M-A. 2004. Scale development in fish: a review, with description of *sonic hedgehog* (*shh*) expression in the zebrafish (*Danio rerio*). International Journal of Developmental Biology 48:233-247.

Sire J-Y, Donoghue PCJ, Vickaryous MK. 2009. Origin and evolution of the integumentary skeleton in non-tetrapod vertebrates. Journal of Anatomy 214:409-440.

Sire J-Y, Huysseune A. 2003. Formation of dermal skeletal and dental tissues in fish: a comparative and evolutionary approach. Biological Reviews 78:219-249.

Smith MM, Hall BK. 1993. A developmental model for evolution of the vertebrate exoskeleton and teeth: the role of cranial and trunk neural crest. Evolutionary Biology 27:387-448.

Smith MM, Hobdell MH, Miller WA. 1972. The structure of the scales of *Latimeria chalumnae*. Journal of Zoology 167:501-509.

Smith MM, Sansom IJ. 2000. Evolutionary origins of dentine in the fossil record of early vertebrates: diversity, development and function. In: Teaford MF, Smith MM, Ferguson MWJ, editors. Development, function and evolution of teeth. Cambridge: Cambridge University Press. p 65-81.

Stensiö EA. 1927. The Downtonian and Devonian vertebrates of Spitsbergen. Part 1. Family Cephalaspidae. Skrifter om Svalbard og Nordishavet 12:1-391.

Stensiö EA. 1932. The cephalaspids of Great Britain: British Museum (Natural History). 1-220 p.

Thomson KS. 1977. On the individual history of cosmine and a possible electroreceptive function of the pore-canal system in fossil fishes. In: Andrews SM, Miles RS, Walker AD, editors. Problems in vertebrate evolution. London: Academic Press. p 247-271.

Vatsa A, Breuls RG, Semeins CM, Salmon PL, Smit TH, Klein-Nulend J. 2008. Osteocyte morphology in fibula and calvaria --- is there a role for mechanosensing? Bone 43(3):452-458.

Vickaryous MK, Sire JY. 2009. The integumentary skeleton of tetrapods: origin, evolution, and development. Journal of Anatomy 214(4):441-464.

Wang NZ, Donoghue PCJ, Smith MM, Sansom IJ. 2005. Histology of the galeaspid dermoskeleton and endoskeleton, and the origin and early evolution of the vertebrate cranial endoskeleton. Journal of Vertebrate Paleontology 25(4):745-756.

Wängsjö G. 1946. On the genus *Dartmuthia* Patten, with special reference to the minute structure of the exoskeleton. Uppsala University Bulletin of Geology 31:349-362.

Wängsjö G. 1952. The Downtonian and Devonian vertebrates of Spitsbergen. IX. Morphologic and systematic studies of the Spitsbergen cephalaspids. Norsk Polarinstitutt Skrifter 97:1-615.

Zylberberg L, Meunier F, Laurin M. 2015. A microanatomical and histological study of the postcranial dermal skeleton of the Devonian actinopterygian Cheirolepis canadensis. Acta Palaeontologica Polonica 61:363-376.

Figure captions

Figure 1. A phylogeny of early skeletonising vertebrates showing the current consensus view of the phylogenetic position of osteostracans, including *Trematapis mammillata*.

Figure 2. Existing hypotheses on the 3D histology of the Osteostraci inferred from 2D data. **A**. Block diagram depicting the histology of the cephalic dermal skeleton in the thyestiid *Trematapis mammilata*. Note the deeply buried "sensory canals" (SC: mesh canals and circum+inter-areal canals) and the polarised odontoblasts (DC: "dentine-like canals") in the tubercles. **B.** Block diagram depicting the histology of the cephalic dermal skeleton in the basal benneviaspidan *Waengsjoeaspis excellens*. Note the circum-areal canals (cac) dividing the surface of the dermal skeleton into polygons. This shows the pattern typical of basal osteostracans and zenaspidans. Abbreviations for A: AVC, ascending vascular canal; C, connection between sensory and vascular canal systems; DC, dentine-like canals; ML, middle layer; P, pore of sensory canal system; RC, radiating vascular canals; SC, sensory canal; SL, superficial layer; SVP, subepidermal vascular plexus; T, Tubercle; VS, vascular cavity for vascular sinus. Abbreviations for B: bl, basal layer; cac, circum-areal mucous canal; case, ascending vascular canal; desc, descending vascular canal; dplx, subcutaneous vascular canal plexus; ebc, external branches from the ascending and radiating vascular canals, forming the subepidermal vascular canal plexus; iac, intra-areal mucous canals; mg, partly covered groove of the mucous canal system; ml, middle layer; p, P1, pores of the mucous canal system; radc, radiating vascular canals; sl, superficial layer; splx, subepidermal vascular canal plexus. A from Denison (1947). B from Wängsjö (1952).

Figure 3. Articulated specimen of the osteostracan *Trematapis mammillata* from which histological samples were obtained, and a reconstruction of the cephalothoracic headshield and complete

external anatomy showing the locations of those samples. **A-B.** Articulated specimen before (A) and after (B) acid dissolution of the surrounding matrix [NHM P25008-9]. **C-D**. Approximate locations of dermal elements sampled shown in (C) dorsal view of the headshield and (d) lateral view of the whole body. C-D. Modified from Janvier (1985b). Scale bars: A-B. 2.3mm, C-D. 10mm.

Figure 4. *Trematapis mammilata*, smooth headshield portion. **A.** Transverse virtual thin section showing the superficial layer with polarised canaliculi overlain by a hypermineralised cap, middle layer of concentric lenticular lacunae and basal layer of plywood-like tissue with distinct fibre bundles. Upper inset shows an orthoslice which reveals lamellae in greater detail. Arrowheads show points where concentric lamellae thin out or apparently stop. Lower inset shows a virtual thin section through a pore cavity. The extent of hypermineralised tissue into the pore cavity is clearest in higher resolution scans of the scales. The superficial layer is interpreted as mesodentine overlain by a hypermineralised cap. The middle layer is interpreted as cellular osteonal bone and the basal layer is interpreted as isopedin (see discussion). **B.** Tangential virtual thin section looking down through the superficial layer showing the horizontal canaliculi which bend towards the pore canals. **C.** Horizontal virtual thin section looking down at the sieve plates underlying the lower mesh canals; perforation diameter of the sieve plates decreases in size of the away from the pore cavities. **D-F.** Successive horizontal virtual thin sections cutting through the (D) upper, (E) middle, and (F) lower basal layers respectively. Note the plywood-like construction and maintenance of the same fibre bundle orientation throughout the middle layer thickness. Note also the truncation of the fibre bundles by the basal cavities, the cross shaped gaps in the upper basal layer and the elongate gaps in the lower basal layer. Abbreviations: bc, basal cavities; en, hypermineralised cap; lbl lower basal layer; lcn lower canal network; lmc, lower mesh canals; mbl, middle basal layer; ml, middle layer; pc, pore canal/cavity; pl polarised lacunae; ps sieve plate; scn, superficial canal network; sl, superficial layer; ubl, upper basal layer; umc, upper mesh canal. Scale bar = 100µm in A (110µm in insets), 211µm in B, 165µm in C and 240µm in D.

Figure 5. *Trematapis mammilata*. Surface renderings of small tissue spaces and fibre bundles revealed by thresholding and manual segmentation respectively. **A.** Vertical section showing polarised superficial lacunae, lenticular middle layer lacunae with a concentric arrangement and highly flattened upper basal layer spaces occurring between lamellae **B.** Lateral view of polarised lacunae and canaliculi arising from the superficial canal network. A short canal (pink) oriented towards the polygonal centre emerges from the lower mesh canals and turns superficially to give rise to the superficial canal network. This then leads into the polarised lacunae of the superficial layer. **C.** Vertical section through superficial layer showing the arrangement of polarised lacunae around a

pore cavity (light blue). **D.** Oblique-superficial view of canals and lacunae in the superficial and middle layers. The canaliculi arising from the polarised lacunae are removed for clarity. **E.** Horizontal section through upper basal layer, viewed superficially, showing cross-shaped gaps between criss-crossing fibre bundles. **F.** Vertical section through the middle basal layer showing gaps between fibre bundles. Blobs generally represent linear structures viewed head on. **G.** Superficial-oblique view of criss-crossing spaces which occur between the fibre bundles of the lower basal layer. **H.** Superficial view of overlapping fibre bundles demonstrating the acute angle of intersection and merging of adjacent fibre bundles in the same lamella. **I.** superficial-oblique view of two overlapping fibre bundles showing oval cross section. Yellow = small tissue spaces, light blue = upper mesh canals, pink = superficial canal network + lower mesh canals + lower canal network, green = upper fibre bundle, purple = lower fibre bundle, dark blue = cut point through surface rendering. Abbreviations as in Fig. 1. Scale bar = 9µm in A, 62µm in B, 37.6µm in C, 67µm in D, 67µm in E, 33µm in F, 68µm in G, 122µm in H, 123µm in I.

Figure 6. *Trematapis mammilata*. Surface renderings of the spaces in the smooth portion of the headshield. **A.** Superficial view showing the polygonal network of upper mesh canals, ring shaped superficial canal network giving rise to polarised lacunae and large ramifying canals in the lower middle layer. Basal cavities removed for clarity **B.** Superficial view showing basal cavities with dark holes representing connections to the lower canal network of the middle layer. **C.** Superficial view showing approximate 1-1 correspondence between the mesh canals and the basal cavities. **D.** Basal view of middle layer canals showing large ramifying canals anastomosing with the lower mesh canals. Connections to the basal cavities are shown in green. **E.** Oblique-superficial view of basal cavities showing annulated surface resulting from fibre bundles and arrangement into rows. Middle layer canals in blue. Basal cavities in yellow. Additional abbreviations: lmc, lower mesh canals; rc, primary ramifying canals of the lower canal network; scn, superficial canal network; umc, upper mesh canal. Scale bar = 500µm in A, 891µm in B and C, 884µm in D and 954µm in E.

Figure 7. *Trematapis mammilata*. Surface rendering of the spaces in a single polygon of the smooth portion of the headshield. **A.** Superficial view of the basal cavities showing ridges corresponding to intersecting fibre bundles. **B.** Oblique superficial view of surface rendering and orthogonal orthoslices showing the relationship between the spaces within the headshield and the tissue layers. **C.** Oblique lateral view of upper mesh canals showing points where they arch over connections between the primary ramifying canals and the lower mesh canals. **D.** Superficial view of middle layer canals. Basal cavities removed for clarity. This shows the loop like superficial canal network and smooth texture of the upper mesh canals. **E.** Basal view of D. Note the presence of narrow canals extending towards the

polygonal centre before turning superficially to supply the superficial canal network. Note also the greatly varying width and roughened surface of the lower mesh canals. Blue = upper mesh canals, pink = lower mesh canals + lower canal network + superficial canal network, yellow = basal cavities. Abbreviations: lmc, ; pc, pore canal; prc, ; scn, superficial canal network; src, small canals radiating towards the polygonal centre. Scale bar = 246µm in A, 167µm in B, 285µm in C, 176µm in D, 133µm in E.

Figure 8. *Trematapis mammilata*. Virtual thin sections through the headshield region bearing tubercles. **A.** Vertical section showing increasing polarisation of lacunae and greater thickness of the hypermineralised cap within the tubercle. Note also the thin basal layer. **B.** Upper and lower images show respectively superficial and superficial-oblique views of a virtual thin section through the superficial layer. The tubercle is denoted by the region where the canaliculi become vertical. **C.** Superficial view of sieve plates showing increase in perforation diameter beneath the pore cavity. **D.** Basal-oblique view of volume rendering showing the extent of sieve plate trabeculae onto the walls of the lower mesh canals. Note how the trabeculae show sharp edges on the basal surface. By contrast they are flat on their upper surface. **E.** Superficial view of horizontal virtual thin section showing the sieve plates in their entirety with very few breaks. Scale bar = 304µm in A, 220µm in B, 89µm in C, 164µm in D and 280µm in E.

Figure 9. *Trematapis mammilata*. Virtual thin sections through the posterior angle of the headshield. **A.** Surface rendering showing external morphology in superficial (left) and basal (right) views. Anterior is to the left in the first image. Note the sagittal row of tubercles on the external surface. Note also the extension of the superficial layer onto the posterior underside. Mesial to this are a series of small tubercles on the interior surface. **B.** Virtual thin section through an interior tubercle showing the hypermineralised cap and polarised lacunae. **C.** Sagittal section showing thick hypermineralised cap as a highly attenuating line on the dorsal surface. Arrows point to a region of spheritic mineralization. Note the presence of trabeculae. **D.** Close up of endoskeleton in transverse section (relative to the long axis of the animal) with the interior surface facing upwards. The superficial layer can be seen extending onto the internal surface and overlying a mesh canal to the left. **E.** Oblique slice viewed from above showing polygonal arrangement of mesh canals. **F.** Orthoslice cut out in basal-oblique view showing arrangement of cavities in rows. Note the irregular fabric of the basal tissue to the left, as opposed to the regular plywood fabric to the right. **G.** Horizontal thin section through the endoskeleton showing structure of trabeculae. Additional abbreviations: sph, spheritic mineralization. Scale bar = 1199µm in A, 174µm in B, 502µm in C, 204µm in D, 606µm in E, 297µm in F, 418µm in G.

Figure 10. *Trematapsis mammilata* caudal trunk scale. A. Vertical orthoslice showing superficial and basal layer tissue. Note the discontinuity of the middle layer. Arrowhead show a patch of middle layer tissue. B. Volume rendering of the scale in external view with anterior approximately to the left. Anterior approximately to the left. B and C are viewed from below and flipped to correspond in orientation to B. C. Horizontal virtual thin section through the superficial layer showing the canaliculi extending to the scale margins. D. Horizontal virtual thin section showing sieve plates and mesh canal geometry. E. Close up of a tubercle under the posterior side of the scale with a polarised lacuna and hypermineralised cap. New abbreviations: dm, dorsal margin; lm, posterior margin; or/am, overlapped region/anterior margin; pm, posterior margin. Scale bar = 164µm in A, 353µm in B, C and D and 78µm in E.

Figure 11. *Trematapsis mammilata*. Surface renderings showing canals of the intermediate caudal trunk scale. **A.** Oblique superficial view of basal cavities, overlapped margin to lower left. Inset shows superficial view with mesh canals overlain showing rough correspondence between the two systems. *B.* Oblique superficial view showing the relationships between the canal systems of the scale. Only a single complete mesh canal polygon is present. **C.** Relationship between tissue types and canal systems of the scale. The poor development of the middle layer means that most canals are at least partly embedded in superficial tissue. **D.** Edge-on view of scale with lower margin facing out of the page showing the lack of topological distinction between the canals. **E.** Superficial view with basal cavities removed for clarity. Overlapped margin towards the top. Note how the superficial canal network extends to the scale margins. **F.** Basal view of E showing lack of differentiation between the lower mesh canals, lower canal network and superficial canal network. Breaks in the lower mesh canals result from sediment infill and island removal. Green regions represent connections to the basal cavities. Colour coding as in Figure 7. Scale bar = 283µm in A (606µm for inset) and B, 176µm in C, 193µm in D, 217µm in E and F.

Figure 12. *Trematapsis mammilata*. Trunk scales. Anterior to the right in all figures except D. **A**-**C**. Diamond-shaped caudal trunk scales. **A.** Volume rendering showing scales in external view. **B.** Vertical orthoslice showing thick hollow basal layer and nearly absent middle layer. **C.** Virtual thick section in superficial view showing mesh canals radiating from a single pore cavity. **D-F.** Rhombic caudal trunk scales. **D.** Isosurface in superficial view showing external morphology. **E.** Posterior basal view of scale showing superficial layer extending onto the scale underside giving rise to tubercles. This is seen in all scales. **F.** Vertical orthoslice showing extensively overlapping scales. **G-H.** Rhombic mid-ventral trunk scales. **G.** Isosurface in superficial view showing external morphology. **H.** Vertical

orthoslice showing overlap of scales. **I.** Horizontal slice showing mesh canal polygons throughout the scales. Abbreviations: bl, basal layer; ml, middle layer; sl, superficial layer. Scale bar = 675µm in A, 209µm in B, 325µm in C, 1219µm in D, 1067µm in E, 541µm in G, 1612µm in G, 393µm in H, 1482µm in I.

Figure 13. *Trematapsis mammilata*. Dorsal trunk scale. **A.** Superficial view of volume rendering showing external morphology. **B.** Horizontal slice through the scale showing a bilaterally symmetrical pattern of mesh canals. **C.** Vertical orthoslice taken near the junction between the lower canal network (right) and a lower mesh canal (left). Note the sharp boundary around the lamellae of the right hand canal and the way in which it cuts across the lamellae surrounding the upper mesh canals. This is interpreted as a result of resorption or a line of arrested growth. **D.** Small canal surrounded by brightly attenuating tissue in the overlapped region. **E.** 3D surface renderings of segmented lamellae from C showing the concentric arrangements of la2 (pink) and la1 (blue and green). Green represents lamellae around lower canal network, blue represents lamella inside the lower mesh canal. Pink represents lamella around the upper and lower mesh canals. This lamella forms an opening where the lamellae of the lower canal network pass through. In reality the blue and green lamellae are continuous. **F.** Relationship between lamellae in E to the surrounding tissue. **G.** Vertical orthoslice showing the continuous extent of la1 (white), la2 (green) and la3 (pink) across the scale, supporting the interpretation of their boundaries as lines of arrested growth during centripetal addition of tissue within the scale. Arrowheads point to enameloid on the inside of the pore cavities. Scale bar = 588µm in A, 502µm in B, 127µm in C, 79µm in D, 174µm in E, 165µm in F and 122µm in G.

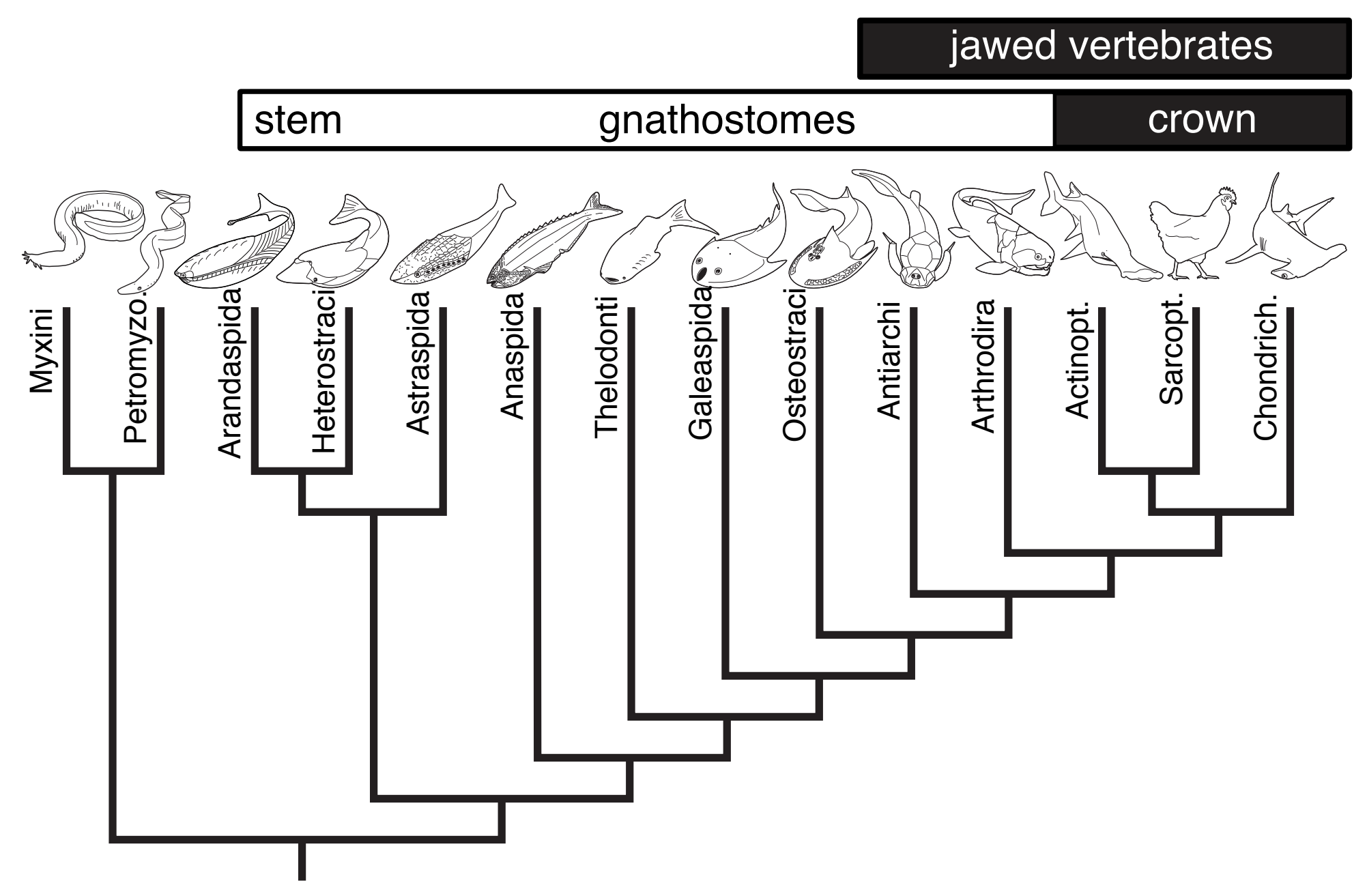
jawed vertebrates
stem
gnathostomes
crown
Myxini
Petromyzo.
Arandaspida
Heterostraci
Astraspida
Anaspida
Thelodonti
Galeaspida
Osteostraci
Antiarchi
Arthrodira
Actinopt.
Sarcopt.
Chondrich.

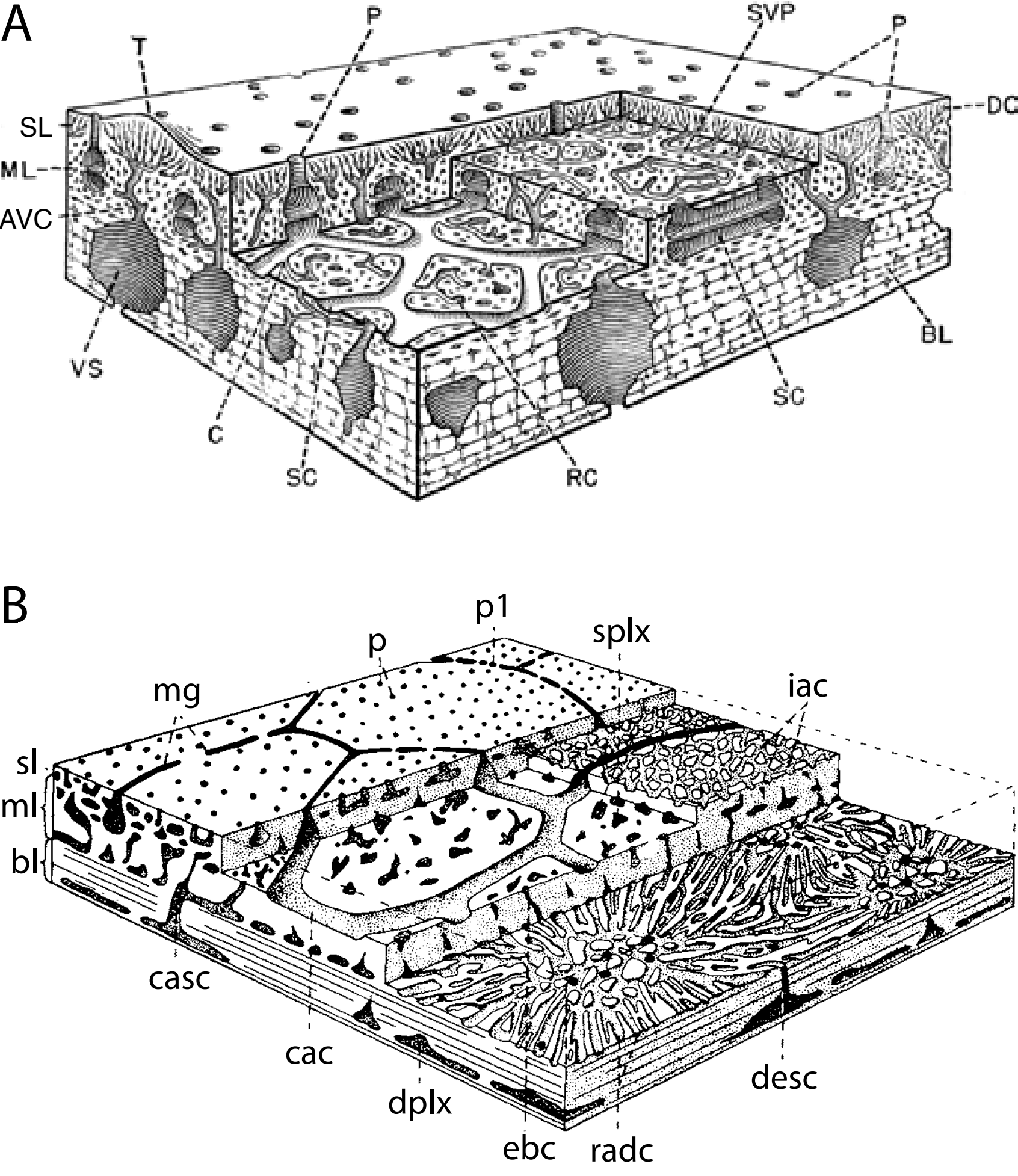
A
T
P
SVP
P
DC
SL
ML
AVC
VS
C
SC
RC
SC
BL
B
p1
p
splx
mg
iac
sl
ml
bl
casc
cac
dplx
ebc
radc
desc

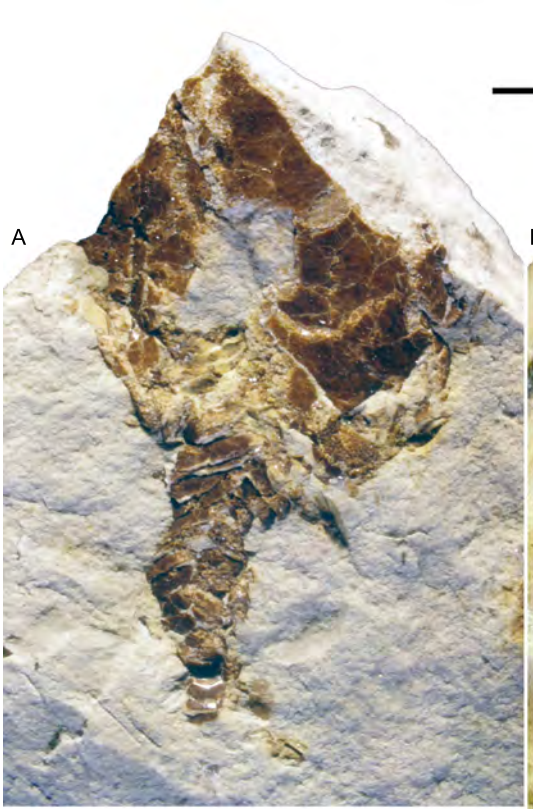
A


B

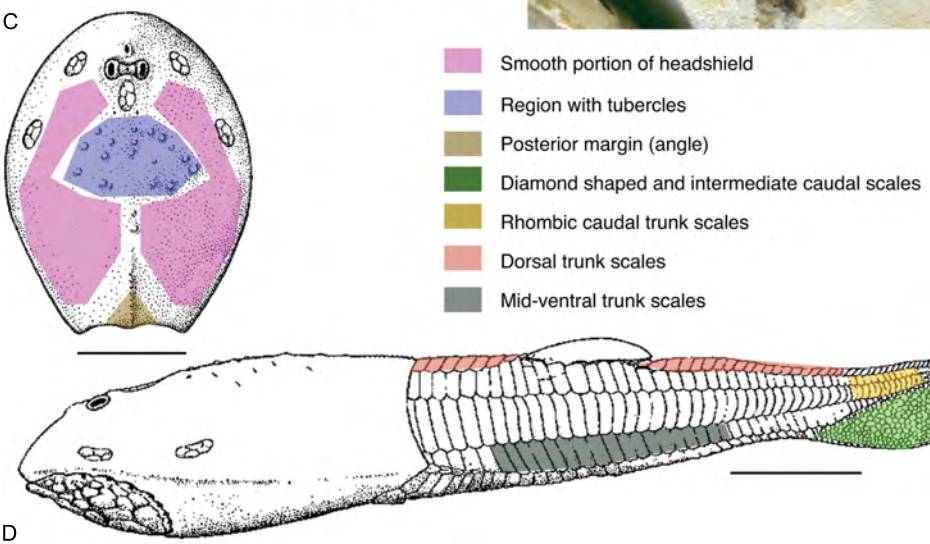
C
Smooth portion of headshield
Region with tubercles
Posterior margin (angle)
Diamond shaped and intermediate caudal scales
Rhombic caudal trunk scales
Dorsal trunk scales
Mid-ventral trunk scales
D

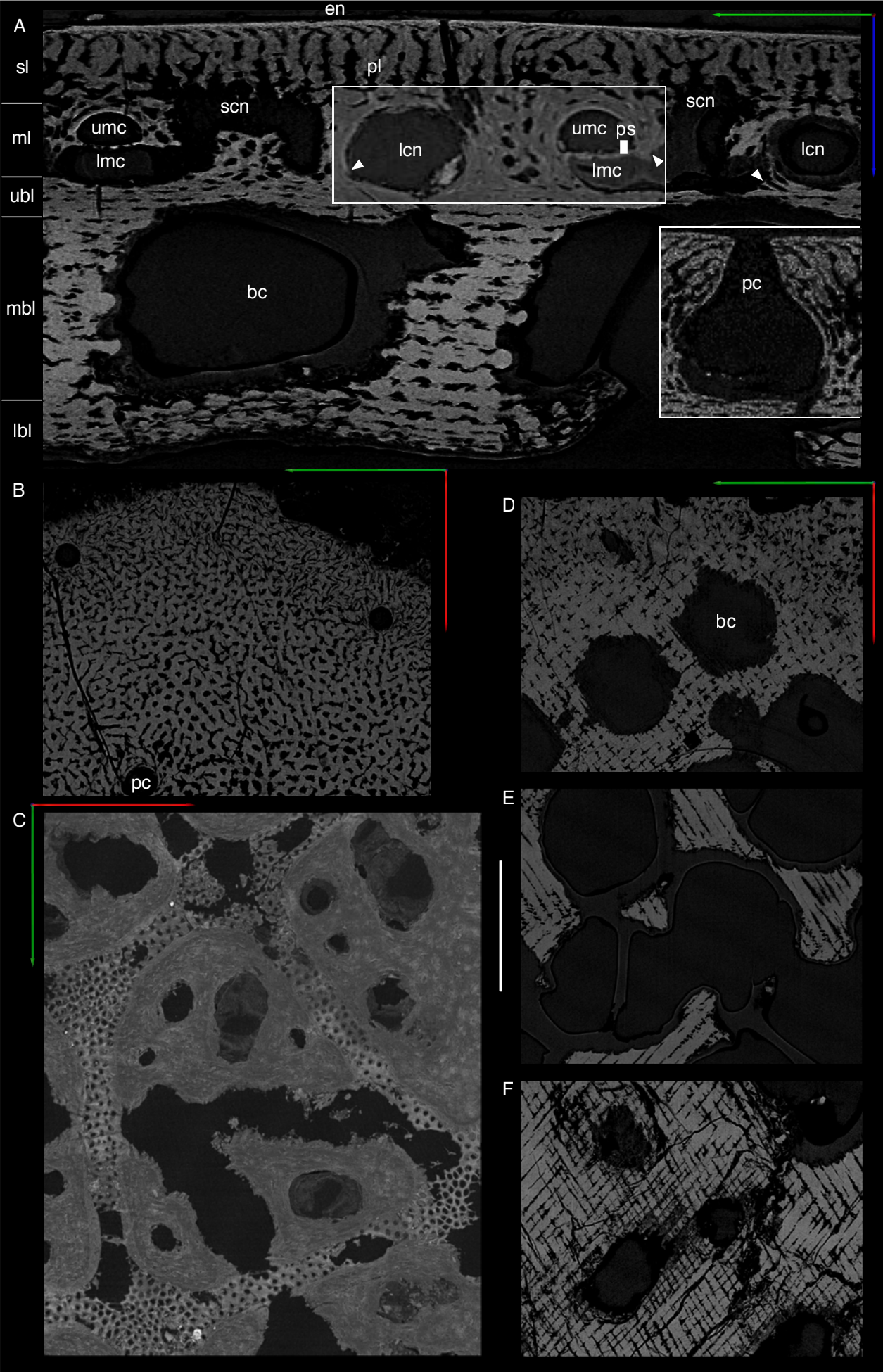
A
en
sl
pl
scn
umc
lmc
ml
ubl
mbl
lbl
bc
lcn
ps
pc
B
C
D
E
F

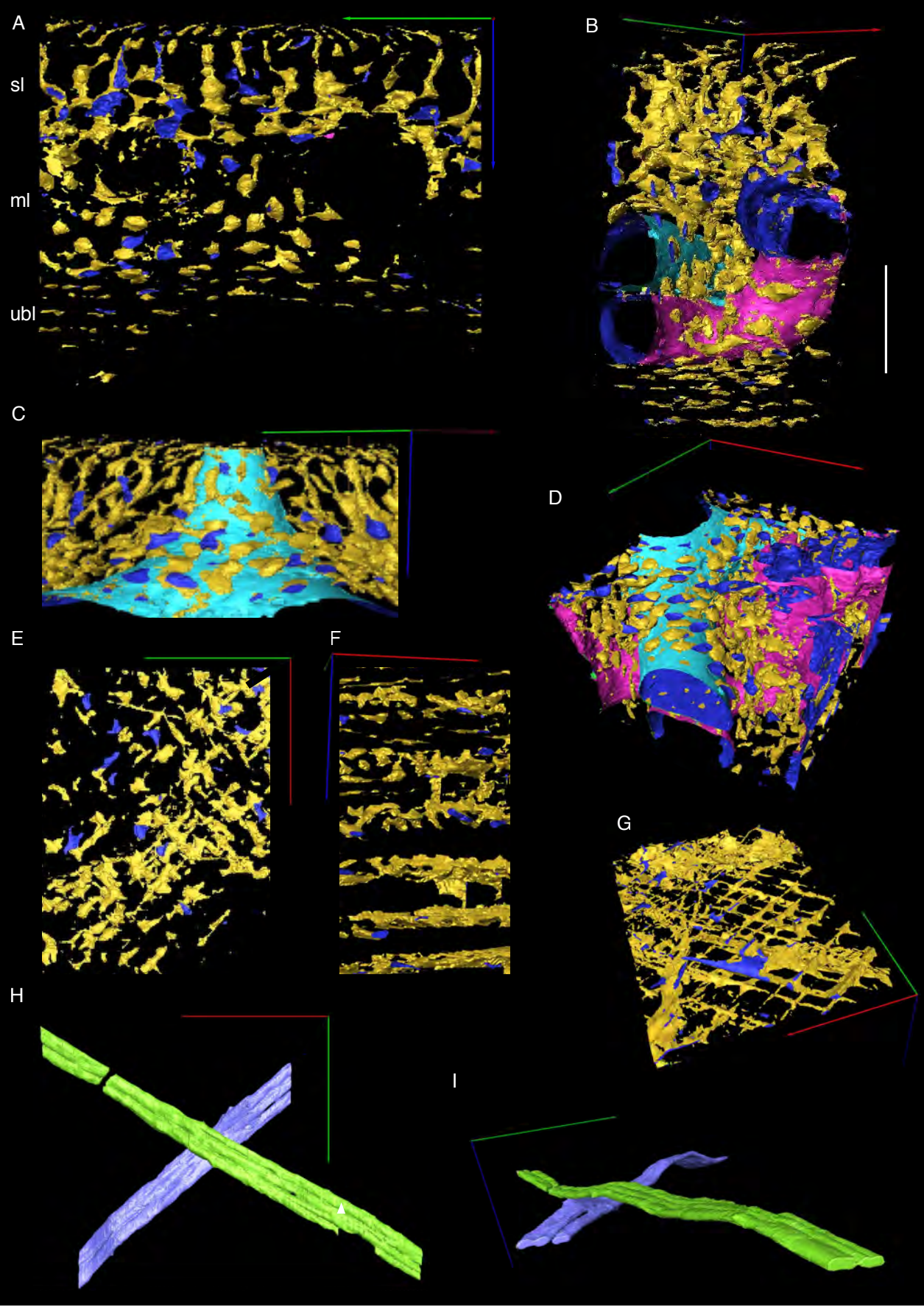
A
sl
ml
ubl
B
C
D
E
F
G
H
I

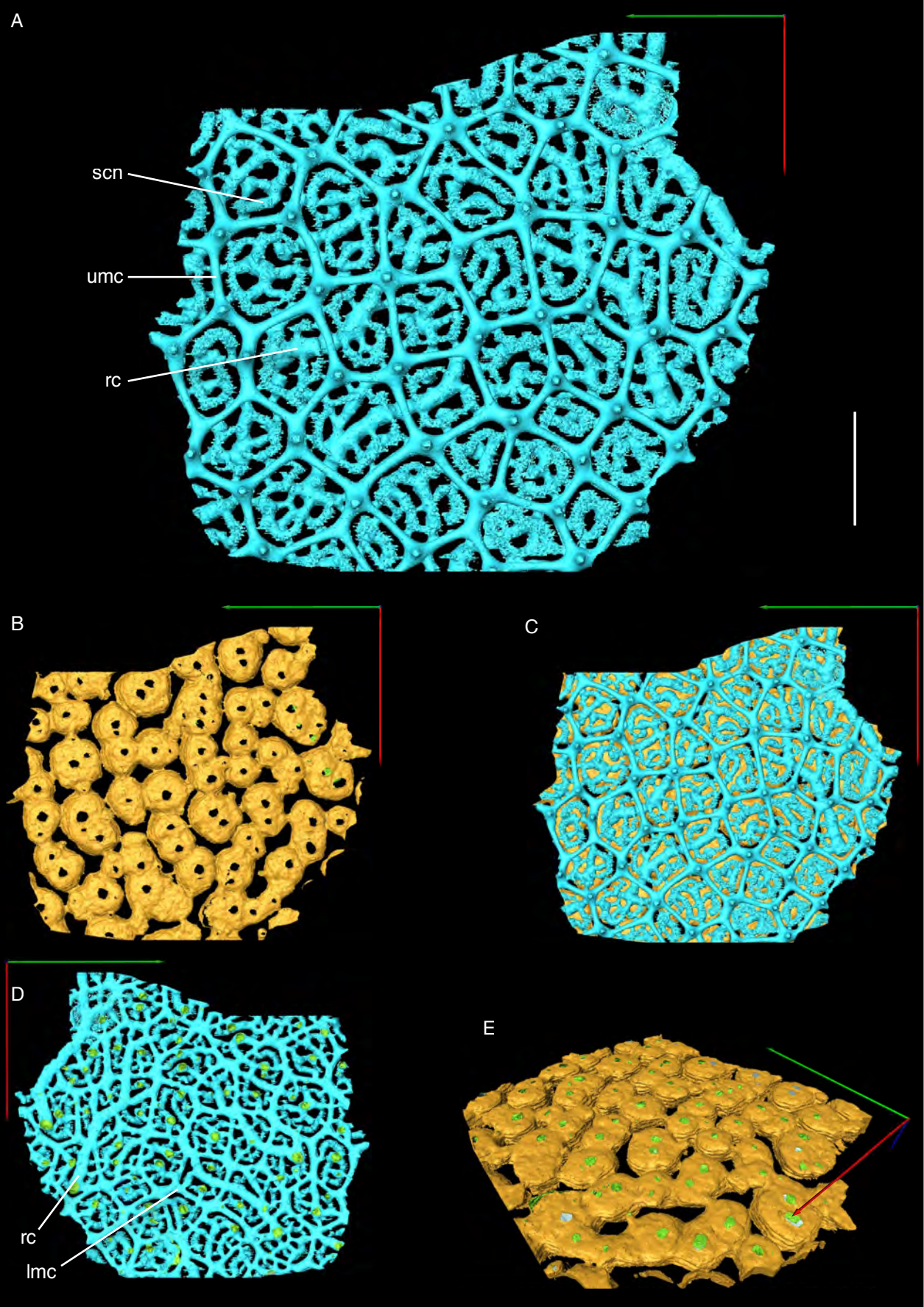
A
scn
umc
rc
B
C
D
rc
lmc
E

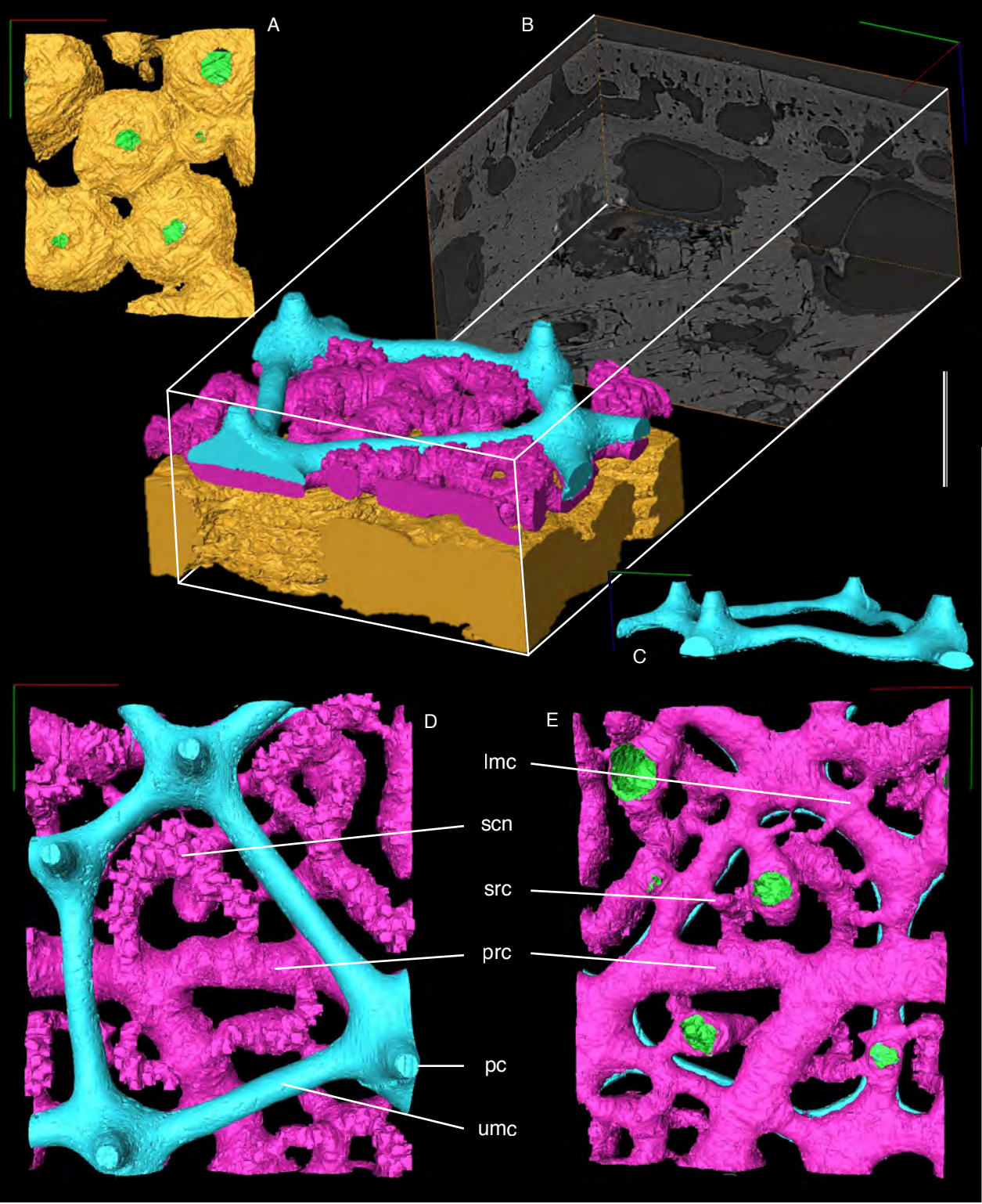
A
B
C
D
E
lmc
scn
src
prc
pc
umc

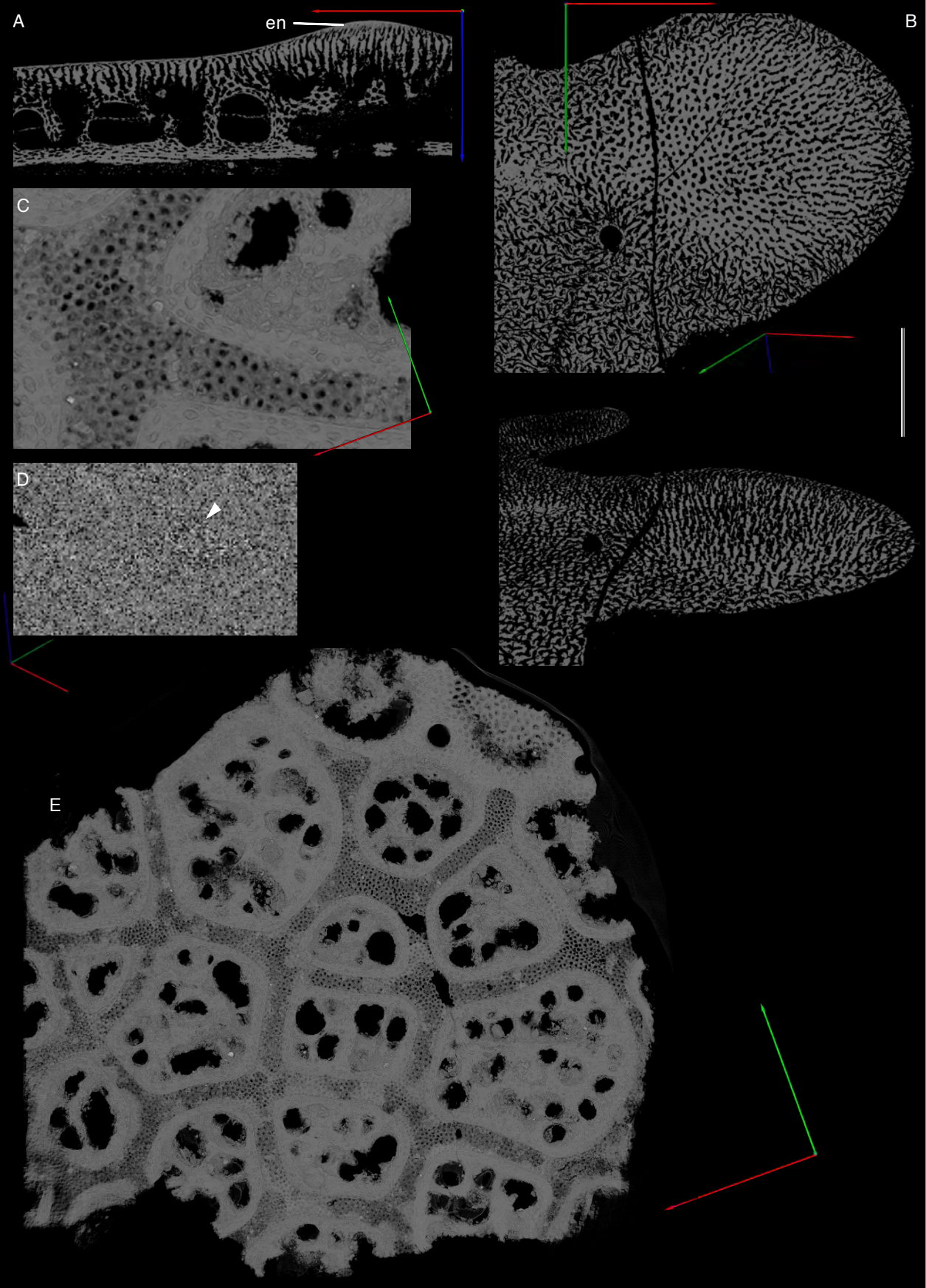
A
en
B
C
D
E

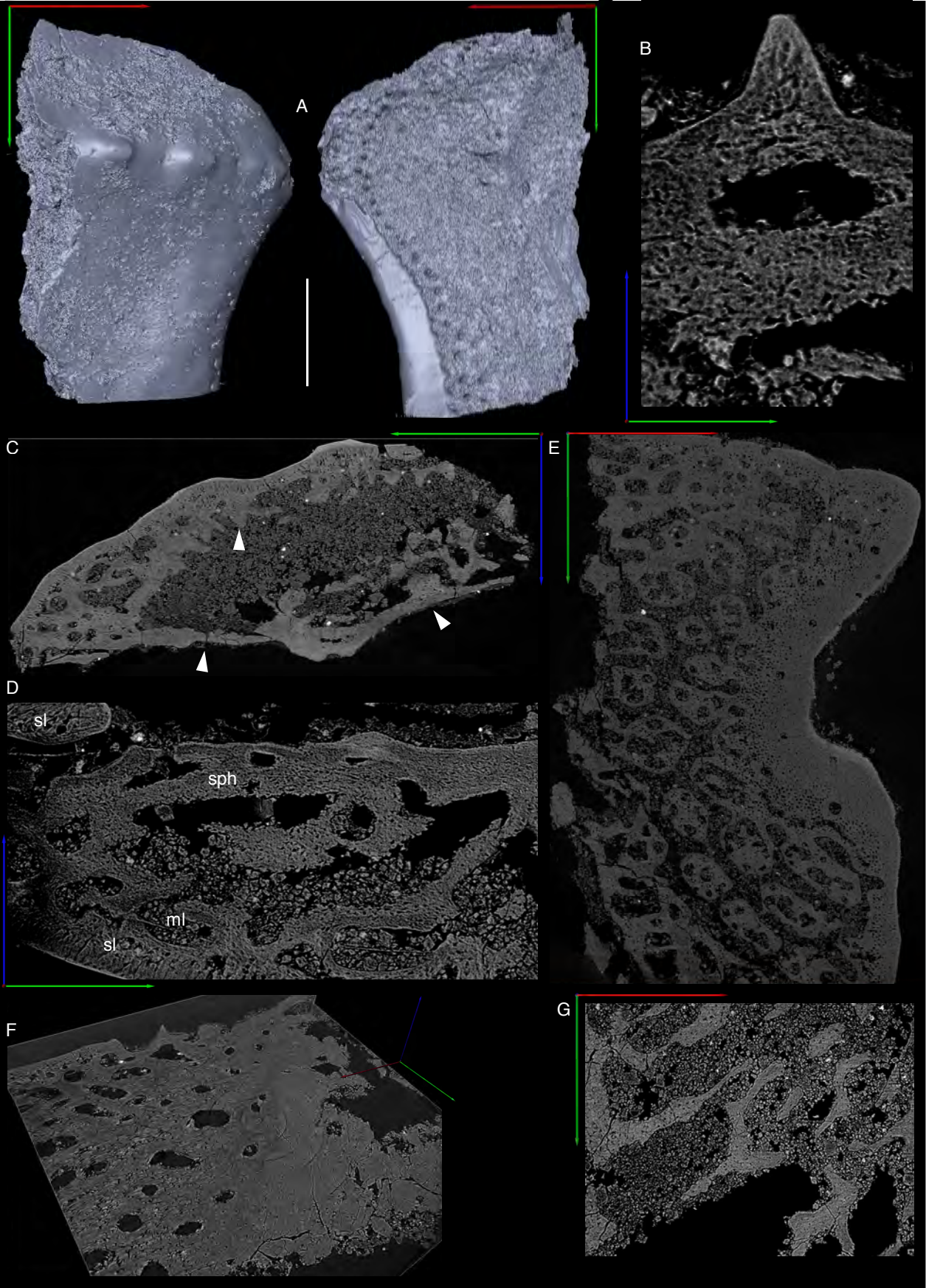
A
B
C
D
sl
sph
ml
sl
E
F
G

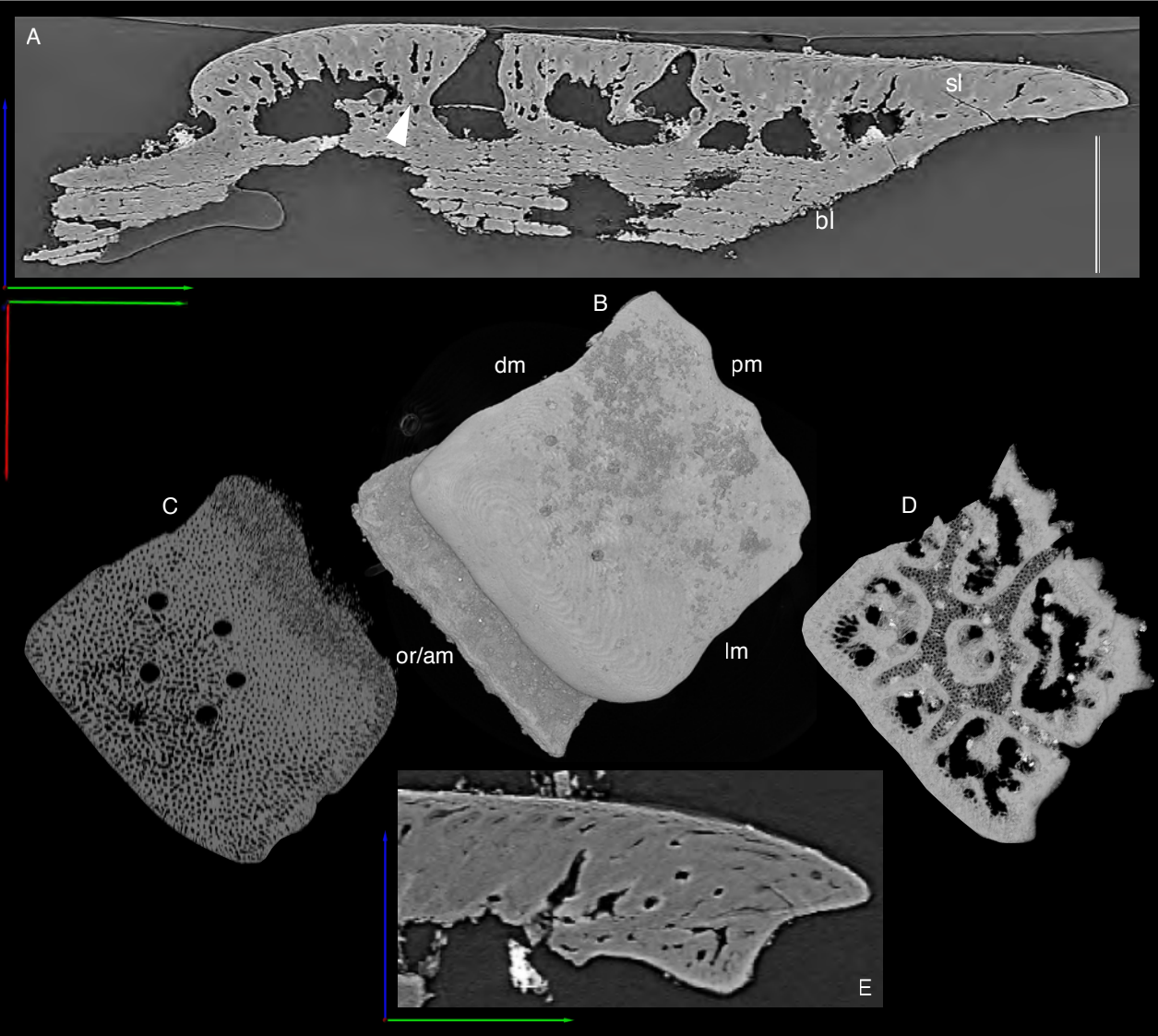
A
sl
bl
B
dm
pm
C
or/am
lm
D
E

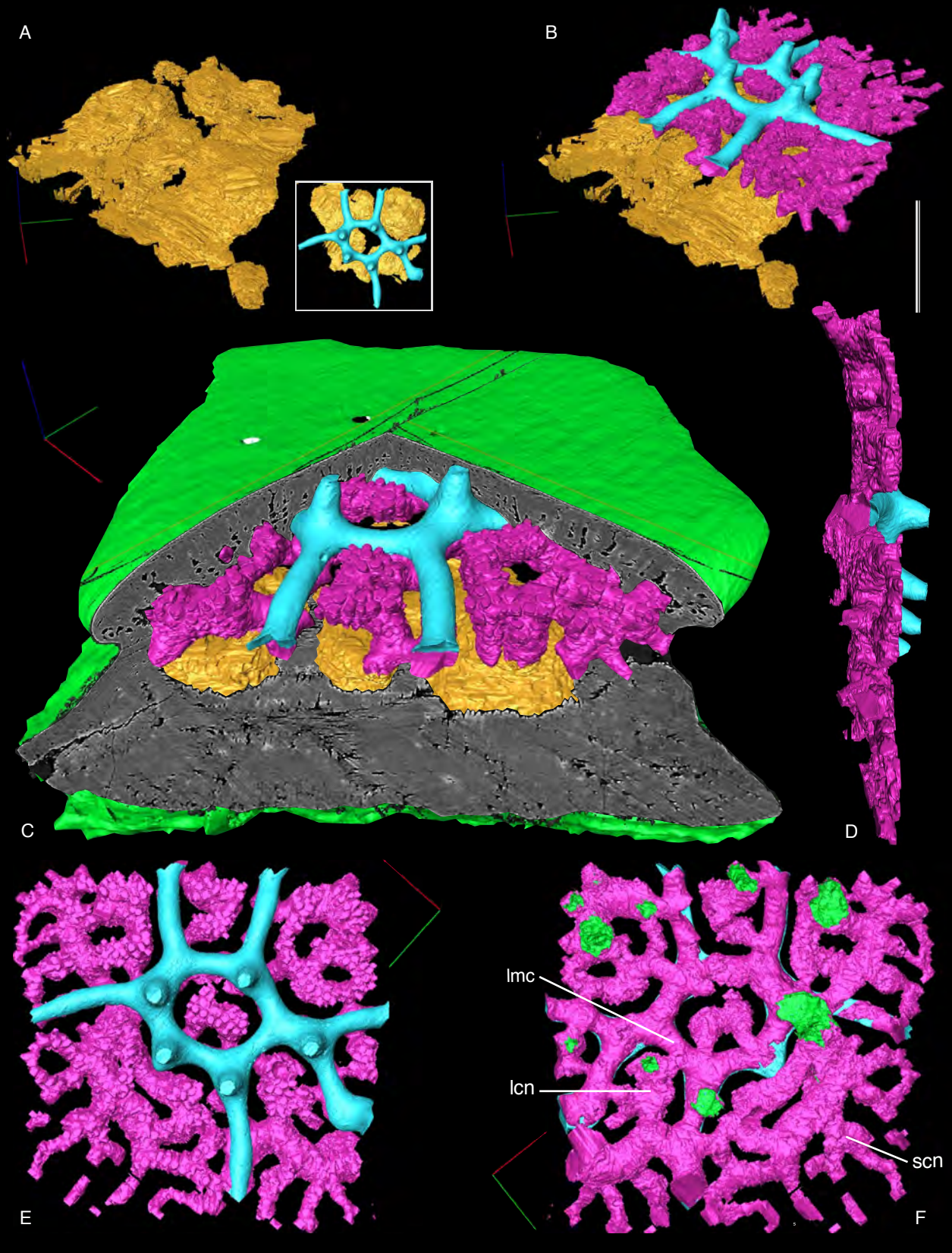
A
B
C
D
E
F
lmc
lcn
scn

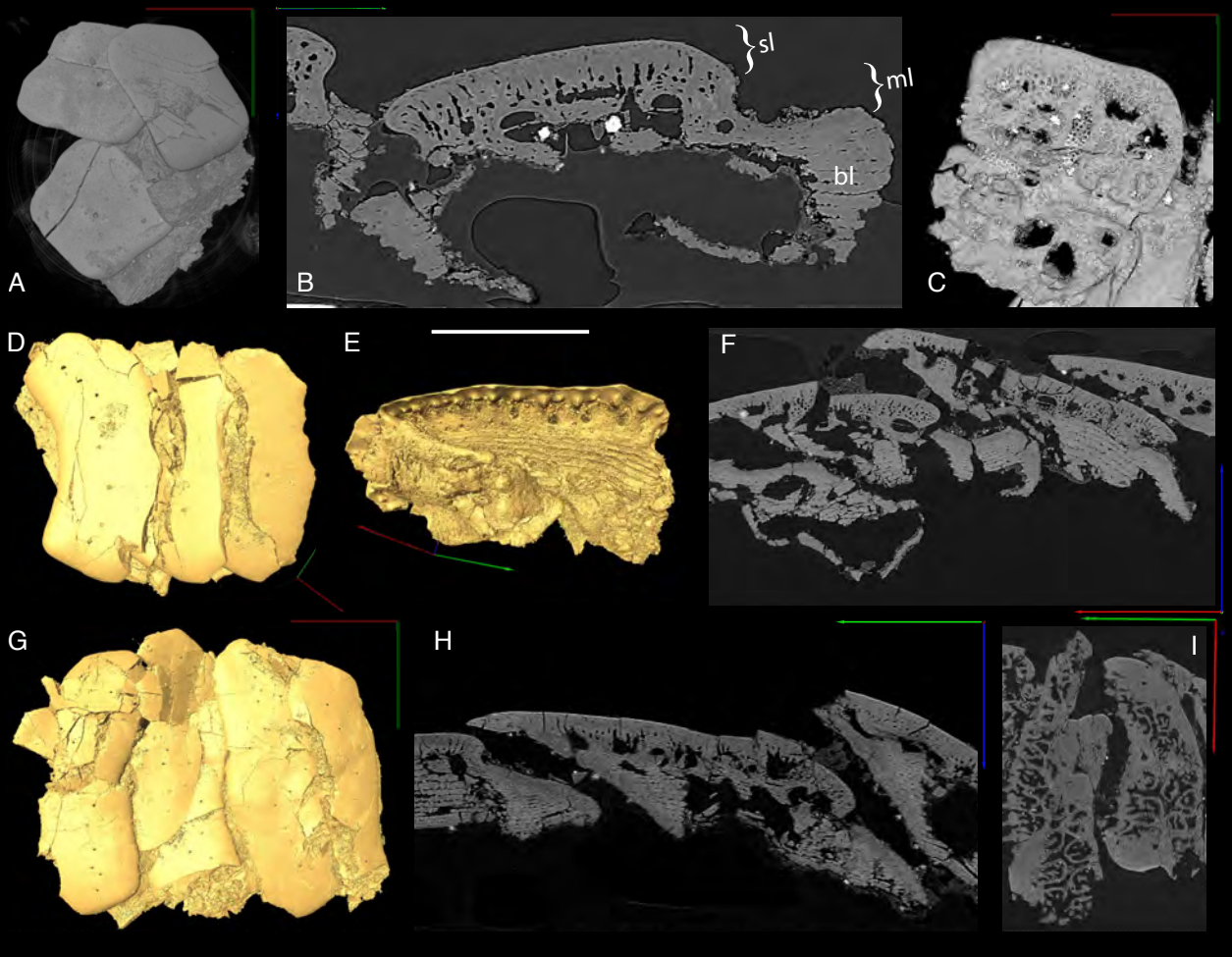
A
B
sl
ml
bl
C
D
E
F
G
H
I

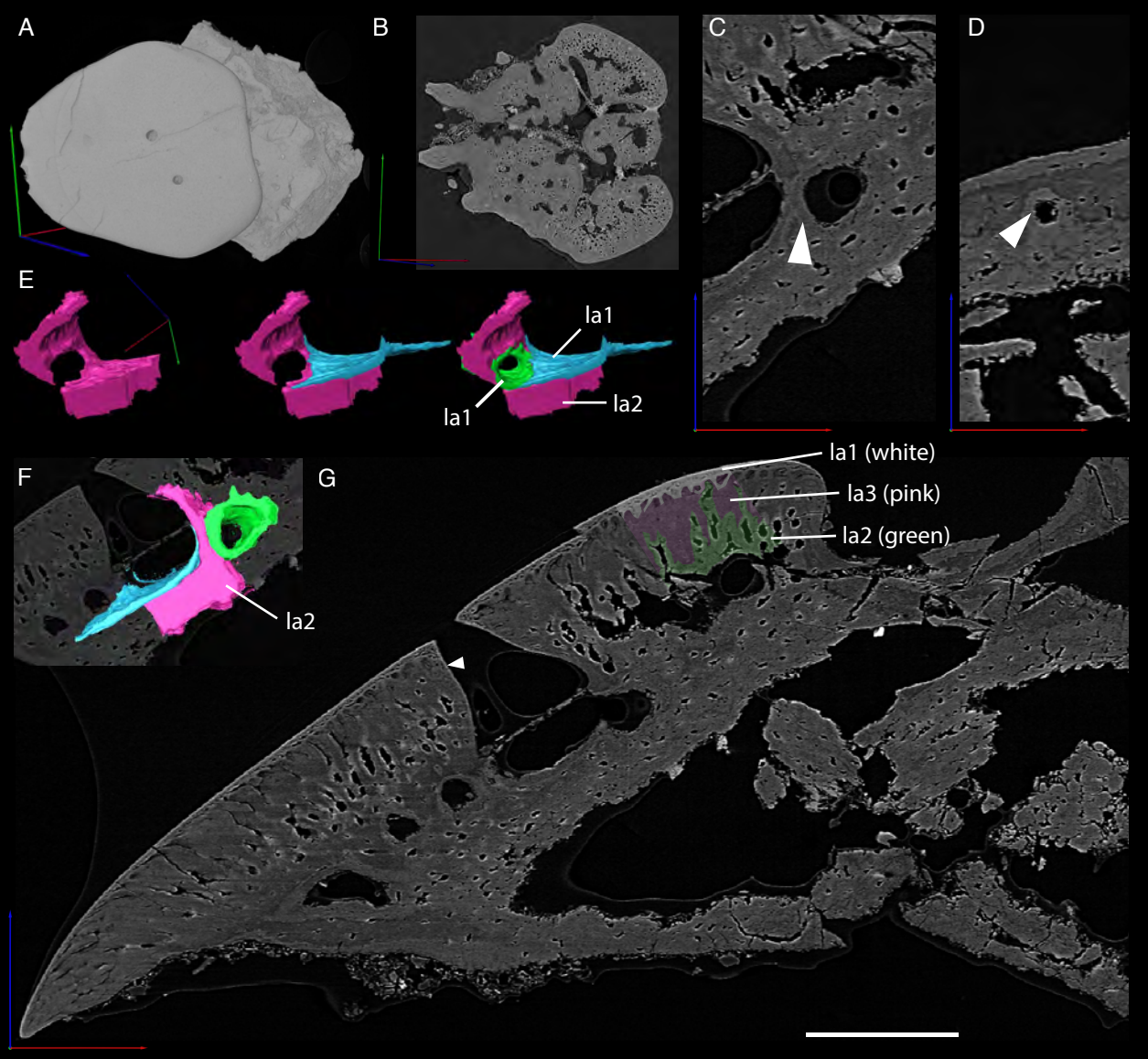
A
B
C
D
E
la1
la1
la2
F
la2
G
la1 (white)
la3 (pink)
la2 (green)